Bulk Transport and Surface Kinetics of Proton Conducting Oxides

Ragnhild Hancke

Dissertation for the degree of Philosophiae Doctor

Department of Chemistry
Faculty of Mathematics and Natural Sciences

UNIVERSITY OF OSLO

April 2013

Preface

This dissertation represents part of the work required for the degree of Philosophiae Doctor (PhD) at the Department of Chemistry, Faculty of Mathematics and Natural Sciences, University of Oslo. The doctoral scholarship has been funded by the research council of Norway through the RENERGI program and the work has been carried out at the Group for Solid State Electrochemistry during the period from September 2009 to May 2013 under the supervision of Associate Professor Reidar Haugsrud, Dr Zuoan Li and Professor Truls Norby.

First of all I wish to thank my main supervisor Reidar Haugsrud for stimulating scientific discussions and for his patience, positivism and encouragements. I'm grateful to co-supervisors Zuoan Li for generously sharing his expertise and experience and Truls Norby for clear-sighted and constructive input at crucial moments. I would also like to express my gratitude to all fellow students and colleagues in the group of Solid State Electrochemistry who has contributed to a great working environment during the past six years. Especially Jonathan and Camilla have become great colleagues and friends. I'm also very grateful to Professor John Kilner and Dr Sarah Fearn for their hospitality and fruitful collaboration during my four months stay at Imperial College in London, 2011.

My warmest feelings and gratitude finally goes out to Amund and my daughter Inga. The support from Amund has been invaluable, and Inga has brought new perspectives on life - as well as work - during the last six months.

Oslo, April 2013

Ragnhild Hancke

Summary

Success in implementing high temperature proton conductors in future energy technologies rests on controlling the transport parameters of the materials in use. When the properties of the bulk materials become better and improved fabrication techniques yield thinner membranes, the demand for fast surface reactions becomes stronger. The surface reaction involves several different steps (adsorption, dissociation, charge transfer etc.), one of which is usually significantly slower than the others and is denoted as the rate determining step. The present work comprises investigations of bulk transport and surface kinetics of proton conducting oxides. The main part of the thesis is concerned with the ternary oxide lanthanum tungstate ($La_{28-x}W_{4+x}O_{54+3x/2}$, generally denoted LWO), whose kinetic properties are compared to state-of-the-art materials with respect to proton and mixed proton-electron conductivity. The main techniques employed to extract the materials' kinetic properties are thermogravimetry (TG), time-of-flight secondary ion mass spectrometry (ToF-SIMS) and gas phase analysis with mass spectrometry.

TG measurements have shown that the oxygen stoichiometry of LWO is essentially constant below 1100 °C, and that the water uptake of the composition with a La/W ratio of 5.6 (LWO56) is significantly larger than that of the tungsten-rich 5.3 composition (LWO53). This is in accordance with the predicted correlation between the cation ratio and inherent oxygen vacancy concentration. The water uptake of LWO56 is, however, still well below the theoretical level, a feature attributed to ordering of the oxygen vacancies at moderate temperatures, effectively decreasing the amount available for hydration. The defect chemical model derived for LWO materials has been successfully fitted to the hydration data, yielding a hydration enthalpy and entropy of -90 kJ mol^{-1} and -115 J $(mol\ K)^{-1}$, respectively. The former is in good agreement with the value -85 kJ mol^{-1} based directly on TG combined with differential scanning calorimetry. The use of H/D isotope exchange experiments for determining the proton concentration and tracer diffusion coefficient has proven to be limited to conditions under which the material is saturated with protons due to the different vapour pressures and hydration thermodynamics of H_2O and D_2O.

Transient TG measurements have been applied to determine the kinetics of proton and water transport in LWO and 10 mol-% Y-doped $BaCeO_3$ (BCO). By employing various sample thicknesses, both the bulk and surface kinetics could be determined. The one-fold hydration of LWO and BCO has been evaluated from the individual contributions of the diffusivity and transport number of protons and oxide ions. The challenges faced when attempting to separate the reduction and oxidation processes constituting the two-fold mass relaxations of BCO under oxidizing conditions have, furthermore, been discussed. The tracer diffusion of protons in BCO is about one order of magnitude faster than that in LWO, and the enthalpy of mobility of protons in the two materials is approximately 43 and 66 kJ mol^{-1}, respectively.

The chemical and tracer surface exchange coefficients of BCO and LWO are of similar magnitudes and have activation energies in the range of 25-50 kJ mol^{-1}. For BCO, the exchange rate increases under reducing conditions compared to that under oxidizing, whereas the activation energy remains unaltered. Based on this behaviour and the functional dependency of the surface exchange coefficients upon water vapour pressure, it has been proposed that the surface exchange rate of BCO is limited by dissociative adsorption of water catalysed by acidic oxygen vacancies. For LWO, the surface exchange under oxidizing conditions has been suggested to be limited by incorporation of hydroxide groups, and, under reducing conditions, we have proposed that H_2 dissociation is involved in the rate determining step. Correlation plots of the surface exchange coefficients and diffusion coefficients reveal a striking similarity between BCO and LWO and support the assumption that oxygen vacancies play a key role in the rate determining steps of their surface exchange reactions.

Ion exchange followed by depth profiling and image mapping with ToF-SIMS has been shown to be a suitable approach to determine tracer transport coefficients of protons and oxide ions, as well as chemical coefficients of water transport. The apparent activation energies of oxygen tracer diffusion and surface exchange on LWO are 176 and 82 kJ mol^{-1}, respectively, and the former likely contains a contribution of the energy associated with oxygen vacancy ordering. The apparent activation energy of proton tracer diffusion in LWO is ~ 63 kJ mol^{-1}, in agreement with the results of transient TG and conductivity measurements. Tracer surface exchange coefficients of protons cannot be determined with acceptable confidence due to a high and irreproducible background of OH^- in the ToF-SIMS. Nominally dry LWO samples hydrated in D_2O contained considerably more shallow

OD^- diffusion fronts than samples subjected to H_2O/D_2O tracer exchange, suggesting that LWO is, indeed, hydrated by ambipolar transport of protons and oxide ions under the applied conditions. Analysis of the surface exchange coefficients indicates that the same mechanism is limiting for surface exchange of oxygen as for the net incorporation of water.

Gas phase analysis of H_2-D_2 isotope couples has been employed to investigate the catalytic activity of LWO-based materials, BCO and 5 mol-% Yb-doped $SrCeO_3$ (SCO) towards hydrogen dissociation and exchange. It appears that point defects play a more important role to the exchange rates than surface defects such as grain boundaries and surface roughness. The exchange rates of unsubstituted and Nd-substituted lanthanum tungstates have activation energies of 90-130 kJ mol^{-1}, whereas the surface exchange on the Mo-substituted specimen displays virtually no temperature dependency. Based on detailed chemical kinetic analyses of the hydrogen pressure dependecies, it has been proposed that adsorption and partial oxidation of hydrogen molecules limits the exchange rate on unsubstituted lanthanum tungstate, whereas the dissociation is rate limiting for the Mo-substituted composition. The H_2-D_2 exchange rates on BCO and SCO surfaces have activation energies of ~ 50 and 130 kJ mol^{-1}, respectively. Their characteristic thicknesses have been estimated based on surface exchange rates and ambipolar conductivities, and is by far greatest for BCO. The critical thickness of SCO has been found to become as low as 0.02 μm in the temperature range relevant for hydrogen separation, whereas it is approximately 30 μm for the lanthanum tungstates.

All together, the characterizations of lanthanum tungstates and acceptor-doped barium cerate and strontium cerate have shown that transient techniques and ToF-SIMS analyses can be successfully combined with the appropriate solutions to Fick's second law to extract phenomenological coefficients for bulk transport and surface kinetics of proton conducting oxides. Gas phase analysis of H-D isotope couples interpreted by combinatorial analysis is, furthermore, a suited technique to probe the oxide surfaces' catalytic activity towards hydrogen adsorption and dissociation.

Table of contents

1. Introduction

In order to slow down global warming and meet a future where utilization of sustainable energy is the preferred alternative, one must find more environment friendly means of combusting fossil fuels and, eventually, come up with apt technologies which are entirely renewable. Hydrogen technologies, relating to the production and use of hydrogen as fuel, have the potential of playing a central role in both these stages of development. The cleanest way to produce hydrogen is from water via electrolysis using for instance sunlight as renewable energy source. However, until the required technologies are implemented, hydrogen may be extracted from fossil fuels, thereby bridging the hydrogen age and the fossil fuel age. Methane, with its high H/C atomic ratio and great abundance in reserves, is an ideal source from which hydrogen may be extracted via steam reformation and water shift, with continuous hydrogen removal through a membrane. This process enables capture and sequestration of CO_2 and produces clean fuel which may be combusted directly to run a steam turbine in a power plant, or be transported and used later in for instance fuel cells where the chemical energy is converted to electricity. A fuel cell may also run on fossil fuels directly, potentially achieving a superior efficiency compared to combustion engines.

Today's leading fuel cells based on water-containing polymers have relatively slow electrode kinetics and a low tolerance to fuel impurities due to a maximum operating temperature of about 100 °C. Solid oxide fuel cells making use of proton conducting ceramic oxides as electrolytes thus comprise an interesting alternative as they operate between 400 and 700 °C and are capable of running on fossil fuels. Ceramic oxides exhibiting *mixed* proton-electron conductivity may, on their side, find use in hydrogen separation technology: Even though palladium-based membranes offer superior hydrogen permeation, they are plagued with sensitivity to surface contamination such as H_2S and CO. Metallic membranes are, furthermore, partly limited to lower temperatures than components based on mixed proton-electron conducting oxides would be, and the high operating temperature of the latter enables thermal integration with other processes such as reformation.

High temperature proton conductivity in perovskite oxides was first reported in 1980 [1], and the excellent proton conducting properties of acceptor doped $SrCeO_3$ and $BaCeO_3$ were soon after discovered and have been extensively studied since [2, 3]. These perovskites still represent the benchmark materials within this class of oxides as they exhibit superior proton conductivity [2-4] and mixed proton-electron conductivity [5-9], respectively. Compared to these materials, the fluorite-related lanthanum tungstate (henceforth denoted LWO) may be considered a newcomer. This material exhibits high and relatively pure proton conductivity below 600 °C as well as mixed ionic-electronic conductivity above 800 °C. Such conductivity characteristics combined with thermal and chemical stability make LWO a potential candidate for both fuel cell and hydrogen separation applications [10, 11]. The material has for instance attracted attention for use in a process where non-oxidative catalytic conversion of methane into aromatics is combined with continuous H_2 removal through a LWO membrane [12]. The above described oxides and the material class they belong to will, from now on, collectively be termed *high temperature proton conductors* (HTPCs).

The level of proton conductivity in HTPCs rests on both the concentration of protons – governed inter alia by the hydration thermodynamics – and their diffusivity, which is expressed by the transport kinetics. Below a certain membrane thickness, the surface exchange rate starts influencing the performance of the material and fast surface kinetics is therefore an important requirement for HTPCs in addition to high proton conductivity. Whereas bulk transport mechanisms are generally well understood, the comprehension of surface exchange processes is rather limited and the literature thereof is sparse.

The primary objective of this thesis has been to measure fundamental kinetic properties of HTPCs with respect to the bulk transport and surface exchange of protons, oxide ions and water, and also to elucidate how these processes are related. A central focus has been to investigate the utility and limitations of various experimental techniques in terms of extracting kinetic properties. Mass- and conductivity relaxations, as well as diffusion profiles recorded with time-of-flight secondary ion mass spectrometry (ToF-SIMS) after isotope exchange annealing, have been analysed according to the appropriate solutions to Fick's second law. Isotopic labelling of gas mixtures combined with mass spectrometry has, furthermore, been employed together with combinatorial analysis to probe the H_2-D_2 exchange rates at the oxide surfaces. The various phenomenological diffusion- and surface

exchange coefficients are sought related throughout this thesis; both with respect to formalism and the fundamental kinetic processes they represent.

Most of the experiments in the thesis have been performed on LWO-based materials. As a candidate material for hydrogen technologies, the properties of this oxide has been particularly addressed only during the last 5 years or so [11], and new knowledge about its crystal structure, stability and transport properties are acquired continually. The topicality of LWO makes analysis of kinetic data more challenging, occasionally being based upon preliminary research which is not fully understood. On the other hand it also strengthens the thesis' impact by providing new insight to a technologically promising material system.

The main part of this thesis consists of 5 manuscripts, and in the following a brief overview of their contents is given:

Manuscript I, *"Thermogravimetric relaxation study of the proton conductor lanthanum tungstate,* $La_{28-x}W_{4+x}O_{54+\delta}v_{2-\delta}$*, x = 0.85"*, focuses on thermogravimetric measurements which record the sample's mass change in response to step changes in water vapour pressure and isotope composition as a function of time under isothermal conditions. Bulk- and surface kinetic properties of H/D tracer exchange and chemical transport of water are thereby extracted, and the manuscript in particular sets out to deconvolute and understand the chemical diffusion coefficient of water.

In Manuscript II, *"Hydration of lanthanum tungstate (La/W = 5.6 and 5.3) studied by TG and simultaneous TG-DSC"*, the compositional responses of lanthanum tungstates to changes in oxygen partial pressure, water vapour partial pressure and H_2O/D_2O is measured, and the data are interpreted and fitted according to the refined structure and defect model. The standard enthalpy of hydration is, furthermore, measured directly by simultaneous thermogravimetry and differential scanning calorimetry.

In Manuscript III, *"The kinetics of hydration and H/D isotope exchange of Y-doped barium cerate and lanthanum tungstate studied by transient thermogravimetry"*, the kinetic characteristics of 10 mol-% Y-doped $BaCeO_3$ are investigated and compared to those of LWO. The applicability of thermogravimetry with respect to differentiating between one-fold and two-fold hydration mechanisms, and the challenges one faces when attempting to curve fit two-fold mass relaxation profiles, is particularly discussed. A more thorough

analysis of the materials' surface exchange mechanism with water is, furthermore, performed by combining chemical kinetics and point defect chemistry.

Manuscript IV, *"Determination of proton- and oxide ion tracer diffusion in lanthanum tungstate (La/W = 5.6) by means of ToF-SIMS"*, presents the results of experiments conducted at Imperial College, London. In this work it is investigated how ToF-SIMS may be applied to characterize the kinetics of HTPCs, using LWO as a model material. In addition to tracer diffusion coefficients of protons and chemical diffusion coefficients of water – parameters which to the best of my knowledge have never been obtained with this technique earlier – tracer diffusion of oxygen is also investigated in this work. Furthermore, the surface exchange coefficient of oxygen tracer exchange and incorporation of water are determined.

Manuscript V, *"Hydrogen surface exchange on proton conducting oxides studied by gas phase analysis with mass spectrometry"* introduces a technique exclusively aimed at characterizing surface exchange processes. The oxide surfaces' interaction with molecular hydrogen is investigated by monitoring the distribution of H and D in the gas phase as a function of time with mass spectrometry. In this manuscript, lanthanum tungstate with various cation substituents, as well as acceptor doped strontium cerate and barium cerate, are characterized with respect to differences in surface morphology and different conditions including temperature, water vapour pressure and hydrogen pressure; the latter dependencies also subjected to a more detailed analysis based on point defect thermodynamics and chemical kinetics. The critical thicknesses of the different materials are, moreover, estimated based on the respective surface exchange rates and ambipolar conductivities.

Before the five manuscripts are presented in full length in Chapter 4, the next chapter introduces the reader to some of the theoretical foundation of the work. The experimental part in Chapter 3 should be considered as supplementary to what have been given in the manuscripts. Here, emphasis is put on ToF-SIMS, thermogravimetry, conductivity relaxation, and gas phase analysis measurements. In Chapter 5 the most important perspectives of the manuscripts are discussed collectively: As the manuscripts have been finished at rather different times, this overall discussion intends to bring them together and allow for new insights. Finally, Chapter 6 offers some concluding remarks.

2. Theory and Background

This chapter treats some of the theoretical foundation for the research in this thesis. Initially I briefly go through the hydration thermodynamics of proton conductors, before moving on to the theory of diffusion and the various phenomenological diffusion coefficients. I thereafter introduce Fick's second law, before discussing surface exchange rates and the potentially limiting effect of surface kinetics on hydrogen permeation through a mixed conducting membrane. Finally, I discuss some general chemical kinetic theories which are important to the interpretation of surface exchange rates.

2.1. Hydration and hydration thermodynamics

The starting point for proton conduction in oxides is generally the presence of oxygen vacancies, usually created in nominally undoped materials by exchange of oxygen between the metal oxide and surrounding atmosphere. These vacancies may be hydrated according to:

$$H_2O(g) + O_O^x + v_O^{\bullet\bullet} = 2OH_O^{\bullet}. \qquad (2.1)$$

Thus, two protonic defects are formed by annihilation of one oxygen vacancy. The equilibrium constant of hydration can be expressed in the following manner:

$$K_{Hydr} = \frac{\left[OH_O^{\bullet}\right]^2}{\left[v_O^{\bullet\bullet}\right]\left[O_O^x\right] p\mathrm{H_2O}} = \exp\frac{\Delta S_{Hydr}^0}{R}\exp\frac{-\Delta H_{Hydr}^0}{RT}, \qquad (2.2)$$

in which ΔS_{Hydr}^0 and ΔH_{Hydr}^0 denote the standard change in entropy and enthalpy upon hydration. The maximum concentration of protons which can be dissolved in an oxide is according to Eq. (2.1) limited by the concentration of oxygen vacancies, which is usually small in nominally undoped materials. It is therefore common to substitute one of the parent cations in the material with one of lower valence (acceptor doping), yielding negatively charged defects whose concentration, commonly designated [$Acc^{/}$], is assumed to be constant. These acceptor dopants are, accordingly, charge compensated by protons and

oxygen vacancies. When the concentration of electronic charge carriers is in minority, the electroneutrality condition of an acceptor doped material can be approximated by:

$$[\mathrm{Acc}^{/}] = [\mathrm{OH}_{\mathrm{O}}^{\bullet}] + 2[\mathrm{v}_{\mathrm{O}}^{\bullet\bullet}], \tag{2.3}$$

where the brackets denote volume concentration or mole fraction. By combining Eq. (2.2) and Eq. (2.3) and assuming that the concentration of protons and oxygen vacancies is small compared to that of oxygen sites (*i.e.* $[\mathrm{O}_{\mathrm{O}}^{\mathrm{x}}] \approx [\mathrm{O}]$), the concentration of protons may be expressed as

$$[\mathrm{OH}_{\mathrm{O}}^{\bullet}] = \frac{[\mathrm{O}]K_{\mathrm{Hydr}}\ p\mathrm{H_2O}\left(-1+\sqrt{1+\dfrac{8[\mathrm{Acc}^{/}]}{[\mathrm{O}]K_{\mathrm{Hydr}}\ p\mathrm{H_2O}}}\right)}{4}. \tag{2.4}$$

It may be noted that the concentration of protons, $[\mathrm{OH}_{\mathrm{O}}^{\bullet}]$, comes out with the same unit as used for $[\mathrm{Acc}^{/}]$ and [O].

2.2. Lanthanum tungstate – Defect structure and hydration

Lanthanum tungstate differs from the above described customary understanding of hydration of oxides in that it is not acceptor doped. The defect structure of LWO, as derived by Erdal et al. [10], is reviewed in the following.

In the most recent structural model for LWO, one formula unit is written $\mathrm{La}_{28-x}\mathrm{W}_{4+x}\mathrm{O}_{54+\frac{3}{2}x}\mathrm{v}_{2-\frac{3}{2}x}$, where x quantifies W on La sites, and v refers to a vacant O site. In the perfect parent structure x = 0, and it is denoted as LWO70 (where the number is the La/W ratio multiplied by 10). This stoichiometry gives two vacant oxygen sites per formula unit. The hypothetical structure of LWO70 is illustrated in Fig. 2.1. Here, all oxygen sites are considered degenerate and the "perfect" oxygen site statistically occupied by 54/56 oxide ions and 2/56 vacancies. This "perfect" site is denoted $\frac{54}{56}\mathrm{O}$. The ideal charge of an oxygen site then comes out as: $\frac{54(-2)+2(0)}{56} = -\frac{108}{56}$. No species carries this exact charge, with the result that the two species natively occupying the O-sublattice are both effectively charged "defects", and we write them $\mathrm{O}_{\frac{54}{56}\mathrm{O}}^{\frac{4}{56}/}$ (an oxide ion) and $\mathrm{v}_{\frac{54}{56}\mathrm{O}}^{\frac{108}{56}\bullet}$ (an oxygen vacancy).

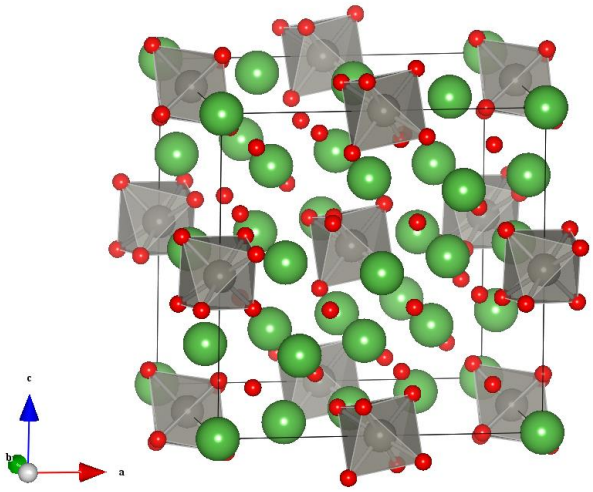

Fig. 2.1: $La_{28-x}W_{4+x}O_{54+\frac{3}{2}x}v_{2-\frac{3}{2}x}$ with x=0 from DFT modeling in VASP by Erdal et al. [10]. Green spheres are lanthanum, grey tungsten and red oxygen.

LWO with La to W ratios at 7.0 or even close to that cannot be synthesized as single phase: The amount of oxygen vacancies appears to be too large [13-15]. As the La to W ratio is decreased below 7.0 and approaches the region of actually synthesizable stoichiometries, a certain amount of W ions substitutes on La sites. XPS analyses, shown in Fig. 2.2, confirm that W remains in its +6 oxidation state. W substituting on La site then forms triply effectively charged donors: $W_{La}^{\bullet\bullet\bullet}$.

If we now consider the stoichiometry with La/W = 5.4, LWO54, x in the above chemical formula equals 1, and one formula unit is therefore written $La_{27}W_5O_{55.5}v_{0.5}$. One W occupies a La-site per unit cell, and 1.5 of the 2 natively vacant oxygen sites are filled, in order to preserve charge neutrality. The concentration of electrons and electron holes are assumed negligible, and the electroneutrality condition can be written as follows:

$$\frac{4}{56}\left[O_{\frac{54}{56}O}^{\frac{4}{56}/}\right]=\frac{52}{56}\left[OH_{\frac{54}{56}O}^{\frac{52}{56}\bullet}\right]+\frac{108}{56}\left[v_{\frac{54}{56}O}^{\frac{108}{56}\bullet}\right]. \qquad (2.5)$$

Notice the analogy to the electroneutrality condition in Eq. (2.3). Also for the lanthanum tungstates, the concentration of vacancies and protons is relatively small compared to the oxygen sites so that $[O_{54/56O}^{4/56/}]\approx[O]$, and hence, an equivalent expression for the proton concentration as given in Eq. (2.4) applies here. In Manuscript II we employ this relation to determine the standard thermodynamic parameters of hydration from thermogravimetric

measurements of the proton concentration in LWO56 as a function of temperature (isobars), and water vapour pressure (isotherms).

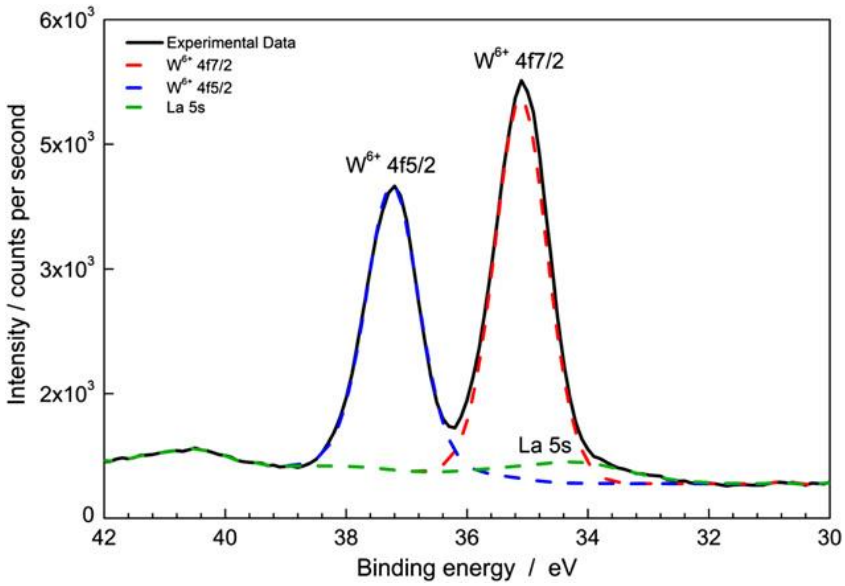

Fig. 2.2: XPS spectra of the W4f5/2 and W4f7/2 regions for LWO53, by Erdal et al. [10]. Only W^{6+} could be detected.

2.3. Self-diffusion

I have so far covered the concentration of the defects, with emphasis on protons, and the related thermodynamics. Equally important to a material's conductivity is the diffusivity, *D*. The Nernst-Einstein equation relates the random or self-diffusivity of the conducting species, *i* to the charge carrier mobility, u_i, the conductivity, σ_i, and the concentration, c_i:

$$D_i = u_i \frac{RT}{nF} = \frac{\sigma_i}{c_i} \frac{RT}{(nF)^2}. \qquad (2.6)$$

The random or self-diffusivity of a particle is generally defined by the jump distance between two adjacent sites, *a*, the jump frequency, ω, and number of available defect lattice sites, N_d, according to:

$$D_i = \alpha a^2 \omega N_d, \qquad (2.7)$$

in which α is a structure dependent factor which for vacancy mechanism may be assumed to be unity. The jump frequency is furthermore determined by the vibrational attempt

frequency, ν, and the thermodynamics of mobility (with subscript *mob*), whereas N_d is defined by the formation thermodynamics of the defect (subscript *f*). The diffusivity is in these terms expressed by:

$$D_i = \alpha a^2 \nu \exp\frac{(\Delta S_{mob} + \Delta S_f)}{R} \exp\frac{-(\Delta H_{mob} + \Delta H_f)}{RT} \ . \qquad (2.8)$$

Here $\alpha a^2 \nu \exp\left((\Delta S_{mob} + \Delta S_f)/R\right)$ may be considered the pre-exponential factor of diffusion. Protons diffuse by the interstitial mechanism and essentially all the nearest neighbour interstitial sites are available for occupancy (*i.e.* $N_d = 1$). Consequently, the formation thermodynamics of protons cancels from Eq. (2.8). The self-diffusion coefficient of protons is denoted $D_{\mathrm{OH}_\mathrm{O}^\bullet}$ in all the manuscripts except for no. IV, in which it for brevity is denoted D_H. The vibrational attempt frequency can be estimated from the enthalpy of defect migration, ΔH_{mob} and the species' mass, M:

$$\nu = \frac{2}{\pi a}\sqrt{\frac{\Delta H_{mob}}{M}} \ . \qquad (2.9)$$

In experiments associated with the kinetics of protons utilizing H_2O-D_2O isotope exchange, it follows that a difference in the pre-exponential factor of proton- and deuteron diffusion of $\sqrt{2}$ must be taken into account. In addition, a so-called semi-classic isotope effect is observed which gives rise to a difference in the activation energy according to:

$$E_{act,D} - E_{act,H} = \frac{1}{2} h(\nu_H - \nu_D) \ . \qquad (2.10)$$

The difference in activation energy of deuterons and protons is estimated to a maximum of ~ 5 kJ mol^{-1} [16].

With the formal definition of the random diffusion coefficient established, I will turn the reader's attention to the *phenomenological* diffusion coefficients, which are those measured by the techniques concerned with in this thesis.

2.4. Tracer diffusion

Tracer diffusion coefficients, D_i^*, are obtained from isotope exchange experiments performed in the absence of a chemical potential gradient. Relevant to this thesis is both

H/D and $^{16}O/^{18}O$ isotope exchange. Tracer diffusion is characterized by not being completely random, but to some extent correlated to previous jumps:

$$D^* = D f^*. \tag{2.11}$$

For vacancy diffusion, f^* is typically 0.5-0.75, whereas for interstitial diffusion, f^* is unity [17].

2.5. Chemical diffusion

The chemical diffusion coefficient, D^δ, in the following exemplified by the chemical diffusion coefficient of water, $D^\delta_{H_2O}$, may be expressed as the proportionality constant between the flux, j_{H_2O}, and concentration gradient in water, formulated in Fick's first law:

$$j_{H_2O} = -D^\delta_{H_2O} \frac{\partial c_{H_2O}}{\partial x}. \tag{2.12}$$

The chemical diffusion coefficient describes the coupled transport of charged species in order to maintain charge neutrality, a phenomenon termed ambipolar diffusion. The flux of water may in these terms be expressed as:

$$j_{H_2O} = -\frac{1}{F^2} \frac{\sigma_{OH_O^\bullet} \sigma_{v_O^{\bullet\bullet}}}{\sigma_{OH_O^\bullet} + \sigma_{v_O^{\bullet\bullet}}} \frac{\partial \mu_{H_2O}}{\partial x}, \tag{2.13}$$

where $\partial \mu_{H_2O} / \partial x$ is the chemical potential gradient of water. From Fick's first law, $D^\delta_{H_2O}$ can be defined as:

$$D^\delta_{H_2O} = \frac{1}{F^2} \frac{\sigma_{OH_O^\bullet} \sigma_{v_O^{\bullet\bullet}}}{\sigma_{OH_O^\bullet} + \sigma_{v_O^{\bullet\bullet}}} \frac{\partial \mu_{H_2O}}{\partial c_{H_2O}} = \frac{RT}{F^2} \frac{\sigma_{OH_O^\bullet} \sigma_{v_O^{\bullet\bullet}}}{\sigma_{OH_O^\bullet} + \sigma_{v_O^{\bullet\bullet}}} \left(2 \frac{\omega_{OH_O^\bullet}}{c_{OH_O^\bullet}} + \frac{\omega_{v_O^{\bullet\bullet}}}{c_{v_O^{\bullet\bullet}}} \right), \tag{2.14}$$

in which ω_i is the so-called thermodynamic factor, accounting for the non-ideality of a diffusion system and defined as $\partial \ln a_i / \partial \ln c_i$. For a diluted system, the thermodynamic factors are often assumed to be unity [4]. By employing the Nernst-Einstein relation expressed in Eq. (2.6) and recognizing that a species' transport number, t_i is defined as σ_i / σ_{tot}, the chemical diffusion coefficient of water in a material whose conductivity is governed by protons and oxygen vacancies may alternatively be expressed as:

$$D^{\delta}_{H_2O} = D_{OH^{\bullet}_O} t_{v^{\bullet\bullet}_O} + D_{v^{\bullet\bullet}_O} t_{OH^{\bullet}_O} , \qquad (2.15)$$

showing that $D^{\delta}_{H_2O}$ is a weighted mean of the individual self-diffusivities of protons and oxygen vacancies. Materials with a substantial concentration of electronic charge carriers do not hydrate by such ambipolar diffusion of protons and oxide ions, but rather in two separate steps of reduction and oxidation, with electronic defects maintaining charge neutrality across the material. The chemical diffusion coefficients of these two processes, in Manuscript III termed D^{δ}_{red} and D^{δ}_{ox}, respectively, may be expressed in equivalent terms as in Eq. (2.15). The principal difference between these two hydration processes has been instructively schematized by Yu et al. [18], reprinted in Fig. 2.3 below.

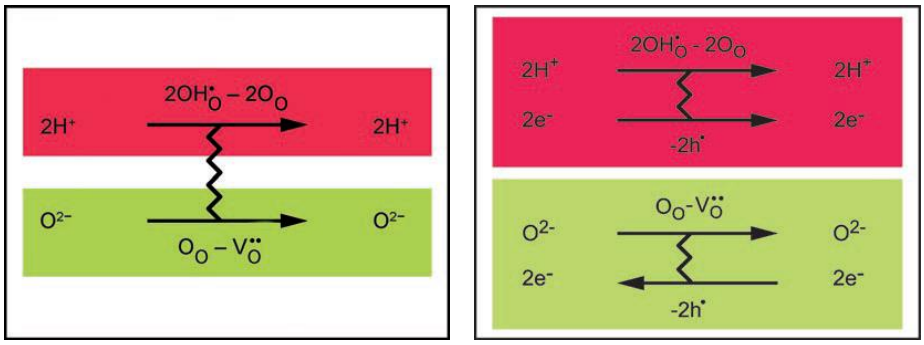

Fig. 2.3: Coupled transport of protons and oxide ions (left) and decoupled transport with electroneutrality maintained by electronic carriers (right), by Yu et al. [18].

2.6. Fick's second law

Fick's second law expresses the situation encountered during transient experiments, *i.e.* when the concentration of a species changes as a function of time:

$$\frac{\partial c_{H_2O}}{\partial t} = D^{\delta}_{H_2O} \frac{\partial^2 c_{H_2O}}{\partial x^2} , \qquad (2.16)$$

here exemplified by a change in the concentration of water, yielding the chemical diffusion coefficient. Solutions to this differential equation are derived by Crank [19] for various boundary conditions. The boundary condition in common for the transient experiments performed in this thesis (thermogravimetry, conductivity and ToF-SIMS) is that the bulk flux, expressed by Fick's first law, is proportional to the concentration difference at the start

(c^S) and end of the interface (first bulk layer, c^B). The flux through the surface region is, consequently, proportional the phenomenological surface exchange coefficient, k. This principle is included in the illustration in Fig. 2.4 and may mathematically be expressed as:

$$-D^{\delta}_{\mathrm{H_2O}} \frac{\partial c_{\mathrm{H_2O}}}{\partial x} = k^{\delta}(c^{S}_{\mathrm{H_2O}} - c^{B}_{\mathrm{H_2O}}) . \qquad (2.17)$$

Furthermore, various geometric boundary conditions apply when solving Fick's second law. By way of example, a flat thin sheet with thickness l is considered for the mass relaxation experiments. By equating the change in hydration level to changes in the sample mass, it is possible to express the thermogravimetric transient as

$$\frac{m(t)-m(0)}{m(\infty)-m(0)} = 1 - \sum_{n=1}^{\infty} \frac{2L_b^2 \exp(-\frac{b_n^2 D^{\delta}_{H_2O} t}{l^2})}{b_n^2(b_n^2 + L_b^2 + L_b)}, \qquad (2.18)$$

where $m(0)$, $m(t)$ and $m(\infty)$ denote the sample mass at the initial time, time t, and infinite time, respectively, and l is the diffusion length (half of the sample thickness). The b_ns are the positive roots of $b_n \tan b_n = lk^{\delta} / D^{\delta}_{H_2O} = L_b$.

By analogy to the diffusion coefficient, the nature of the extracted surface exchange coefficient depends on the type of experiments performed. The chemical surface exchange coefficient is related to the tracer surface exchange coefficient, k^*, by the thermodynamic factor, ω:

$$k^*/k^{\delta} = \omega^{-1} \qquad (2.19)$$

in which ω is defined as before.

2.7. Surface exchange rate

The definition and treatment of flux has insofar concerned the flux of water, for the purpose of defining the most relevant chemical diffusion coefficient to this thesis ($D^{\delta}_{\mathrm{H_2O}}$). As we turn our attention to surface exchange rates, we will move on to the transport of H_2 through a membrane, described by equations based on Bouwmeester's [20] treatment of oxygen permeation membranes.

A gas separation membrane may be divided into a central bulk zone and two adjacent interfacial zones, as schematized in Fig. 2.4.

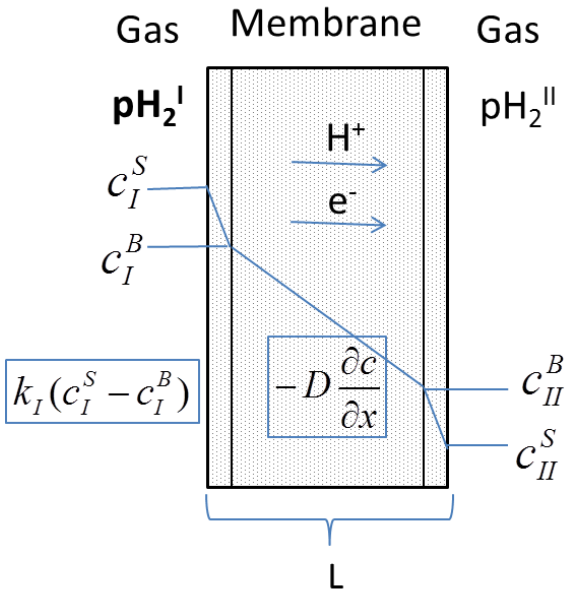

Fig. 2.4: Schematic illustration of a hydrogen separation membrane. The total driving force for hydrogen transport is the difference in hydrogen partial pressure at the two sides of the membrane. A part of the driving force is used to support the bulk diffusion and the remaining to support the two surface reactions.

The flux of hydrogen through bulk may be expressed in equivalent terms to that in Eq. (2.13), and we note that when the expression is integrated over the thickness of the membrane, *L*, the bulk hydrogen flux is expressed as:

$$j_{\mathrm{H_2}} = -\frac{t_{\mathrm{e'}} t_{\mathrm{OH_O^\bullet}} \sigma_{total} \Delta\mu_{\mathrm{H_2}}^{bulk}}{2^2 F^2 L}, \qquad (2.20)$$

where $\Delta\mu_{\mathrm{H_2}}^{bulk}$ is the drop in chemical potential of hydrogen across the bulk. The flux of hydrogen through the gas-solid interface may, at conditions close to equilibrium, be expressed as:

$$j_{\mathrm{H_2}} = -j_{ex}^0 \frac{\Delta\mu_{\mathrm{H_2}}^{\mathrm{int}}}{RT}. \qquad (2.21)$$

Here, $\Delta\mu_{H_2}^{int}$ is the chemical potential drop across the gas/solid interface. The quantity j_{ex}^0 (mol H_2 cm^{-2} s^{-1}) denotes the balanced exchange rate in the absence of hydrogen potential gradients and is related to the surface exchange coefficient k_s (cm s^{-1}) through:

$$j_{ex}^0 = \frac{1}{4} k_s c_{OH_O^\bullet} \tag{2.22}$$

where $c_{OH_O^\bullet}$ is the bulk concentration of hydrogen.

2.8. Critical thickness – surface vs. bulk control

Bulk diffusion typically dominates the transport rate when the membrane thickness is large, but as the thickness decreases the transfer across the interfaces becomes rate determining. It can be shown that the critical thickness of the membrane is expressed by:

$$L_C = \frac{RT}{2^2 F^2} \frac{t_{e'} t_{OH_O^\bullet} \sigma_{total}}{j_{ex}^0}. \tag{2.23}$$

For predominant electronic conduction, *i.e.* $t_{e'} \approx 1$, a combination of this expression with the Nernst-Einstein equation and the relation expressed in Eq. (2.22) yields an alternative representation of the critical thickness for two equally limiting surfaces:

$$L_C = 2D_{OH_O^\bullet} / k_s. \tag{2.24}$$

When the membrane thickness, L, is far larger than L_C, the hydrogen flux varies inversely with the membrane thickness, but deviations from this inverse relationship are observed when the hydrogen flux becomes partly governed by the surface exchange kinetics. Eventually, when $L<<L_C$, the flux becomes independent of the membrane thickness. In Fig. 2.5 left and right, Lenhardt et al. [21] experimentally show the two kinetic extremes where the transport is predominantly diffusion controlled and surface controlled, respectively. The profiles are recorded in-situ for Fe-doped $SrTiO_3$ by optical absorption spectroscopy, illustrating how the diffusion profiles will penetrate through a sample from two sides in the two limiting cases.

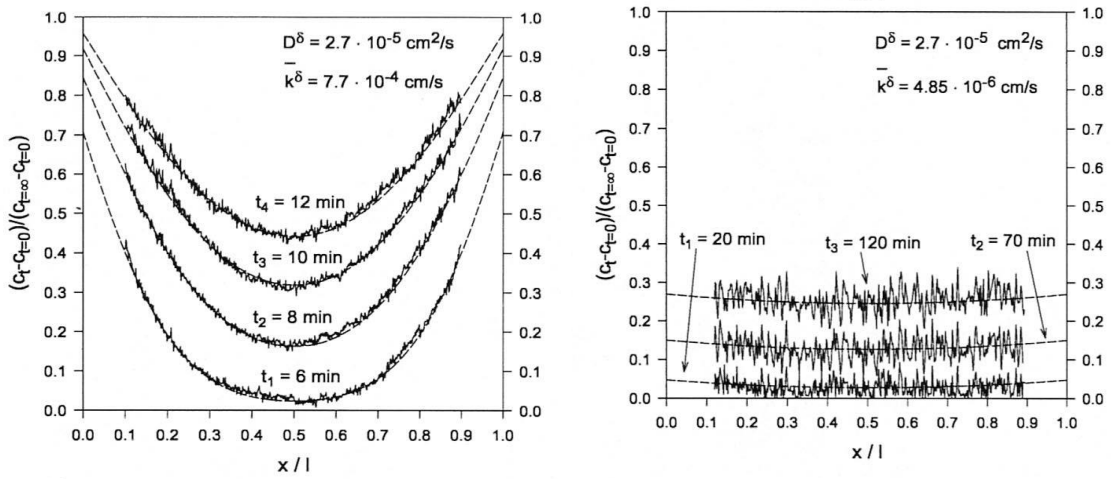

Fig. 2.5: Oxygen incorporation experiments in Fe-doped $SrTiO_3$ single crystals followed by in-situ time and space resolved optical absorption spectroscopy, by Lenhardt et al. [21]. Left: Predominantly diffusion controlled case, right: Predominantly surface controlled case. The materials only differ in surface treatment.

2.9. The surface exchange reaction – chemical kinetic analysis

A brief overview of the chemical kinetic theory underlying the discussion in Manuscript III and V is provided in the following, using the reaction with hydrogen as example. For dissociative adsorption of H_2 on an oxide surface, the Langmuir isotherm expresses the relation between the coverage of hydrogen, θ_H, and the hydrogen partial pressure and thermodynamics of dissociative adsorption, through the equilibrium constant K_{H_2}:

$$\theta_H = \frac{(K_{H_2} pH_2)^{\frac{1}{2}}}{1+(K_{H_2} pH_2)^{\frac{1}{2}}}. \qquad (2.25)$$

For the kinetic treatment herein, low surface coverage (1-$\theta \approx 1$) is assumed. In Manuscript V we propose a reaction mechanism describing adsorption, charge transfer, dissociation and incorporation of hydrogen into an oxide. The reaction is suggested to consist of two sequential reaction steps coupled in series according to:

Step 1: $H_2 = H^{\bullet}_{2,ads} + e^{/}$

Step 2: $H^{\bullet}_{2,ads} + 2O^{x}_{O} = 2OH^{\bullet}_{O} + e^{/}$ (2.26)

If we assume that step 1 is rate-determining and that the others are in quasi-equilibrium, the reaction rate is expressed as:

$$r_1 = r_1^+ - r_1^- = k_1^+ p\mathrm{H}_2 - k_1^- [\mathrm{H}^{\bullet}_{2,\mathrm{ads}}][\mathrm{e}^{/}] \tag{2.27}$$

$$r_1 = r_1^+ - r_1^- = k_1^+ p\mathrm{H}_2 - k_1^- [\mathrm{e}^{/}]^2 [\mathrm{OH}^{\bullet}_{\mathrm{O}}]^2 [\mathrm{O}^{\mathrm{x}}_{\mathrm{O}}]^{-2} K_2^{-1} \tag{2.28}$$

in which r_1^+ and r_1^- are the forward and backward reaction rates, k_1^+ and k_1^- the forward and backward rate constants, and K_2 the mass action constant of step 2 [17]. At, or close to, equilibrium – which is the condition dealt with in this thesis - the net rate is zero ($r_1 = 0$) and the equilibrium reaction rate, R_0, may be expressed as

$$R_0 = \sqrt{r_1^+ r_1^-} = \sqrt{k_1^+ k_1^- K_2^{-1} p\mathrm{H}_2 [\mathrm{e}^{/}]^2 [\mathrm{OH}^{\bullet}_{\mathrm{O}}]^2 [\mathrm{O}^{\mathrm{x}}_{\mathrm{O}}]^{-2}} \,. \tag{2.29}$$

In order to relate the theory of hydrogen flux to chemical kinetics in Manuscript V, the balanced exchange rate, j_{ex}^0 defined in Eq. (2.17), and the equilibrium reaction rate, denoted R_0 herein, are treated as the same quantity. These are furthermore equated to the phenomenological surface exchange rate, R, extracted from the gas phase analysis technique concerned with in Manuscript V and which should not be confused with the gas constant. In the following we describe the theory providing the basis for extraction of the surface exchange rate.

2.10. Combinatorial analysis

Relevant to Manuscript V is combinatorial analysis which can be used for a system of diatomic molecules, *e.g.* for a quantitative description of the exchange of hydrogen between the gas phase and the adsorbed surface state. In Fig. 2.6 we have reprinted a sketch by Hörnlund [22] which illustrates the underlying principle.

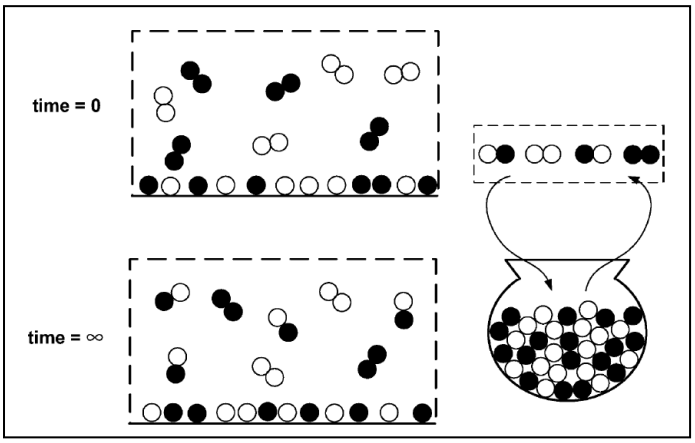

Fig. 2.6: A schematic drawing of a system with two isotopes, by Hörnlund [22]. Assuming identical isotope distribution on the surface and in the gas phase allows the use of combinatorial analysis on the system.

The probability of forming hydrogen molecules with atomic mass *i*, P^i, depends on the isotope composition of the gas phase, and can for the different gaseous hydrogen species H_2, HD and D_2 be expressed by

$$P^2 = \left(\frac{[\mathrm{H}]}{[\mathrm{H}]+[\mathrm{D}]} \right)^2$$

$$P^3 = 2\frac{[\mathrm{H}][\mathrm{D}]}{([\mathrm{H}]+[\mathrm{D}])^2} \qquad (2.30)$$

$$P^4 = \left(\frac{[\mathrm{D}]}{[\mathrm{H}]+[\mathrm{D}]} \right)^2$$

The concentration of each molecular hydrogen species at statistical equilibrium, c^i_{eq}, is given by

$$c^i_{eq} = P^i n, \qquad (2.31)$$

where *n* is the total amount of hydrogen gas in the reaction chamber.

By assuming that the [H]/[D]-ratio is identical at the surface and in the gas phase, the rate at which the gas phase concentration of a specific molecule changes may be calculated from the rate of adsorption r_i^+ and the rate of desorption r_i^- of the molecule. These are given by

$$r_i^+ = P^i R \frac{c^i(t)}{c^i_{eq}} \qquad (2.32)$$

$$r_i^- = P^i R \tag{2.33}$$

where $c^i(t)$ is the number of moles of each molecular species at equilibration time t and R is the total exchange rate of molecular species between the gas phase and the surface state (with the unit mol H_2 cm^{-2} s^{-1}). The rate at which the concentration of molecule i changes is then given by

$$\frac{dc^i}{dt} = r_i^- - r_i^+ = \frac{RS}{n}(c_{eq}^i - c^i(t)), \tag{2.34}$$

where S denotes the surface area of the specimen. This equation may be integrated to yield:

$$c(t) = c_{eq} + (c_0 - c_{eq})\exp\left(-\frac{RSt}{n}\right) \tag{2.35}$$

Here c_0 is the concentration of each species at $t = 0$.

3. Methodology

This chapter gives experimental details supplementary to those described in the individual manuscripts. The instrumentation of time-of-flight secondary ion mass spectrometry, thermogravimetry, conductivity relaxation measurements and gas phase analysis with mass spectrometry is particularly focused on.

3.1. ToF-SIMS

Manuscript III treats the analyses of diffusion profiles in LWO by time-of-flight secondary ion mass spectrometry (ToF-SIMS). In the following, the isotope exchange rig, the ToF-SIMS instrument and the recording of images and depth profiles are described.

3.1.1. Exchange rig

The ToF-SIMS analyses were performed on diffusion profiles which were induced by treating the samples in a specially designed exchange rig, shown in Fig. 3.1 [23]. Silica fingers containing H_2O, D_2O and $H_2{}^{18}O$ were used. These silica fingers were surrounded by a water bath which effectively varies the pressure of the exchange vapour by regulating its temperature. After the desired temperature was reached and the exchange carried out, the water bath was replaced by a liquid nitrogen bath to recover the water vapour. No carrier gas (N_2/H_2 as depicted in the figure) was employed in our experiments.

Due to the fast diffusion of protons in LWO, it was necessary to keep the H_2O-D_2O exchange anneals short (~15 minutes on average) and perform them below 350 °C in order not to violate the assumption of diffusion in a semi-infinite medium. The combination of these annealing conditions and an activation enthalpy of only ~ 65 kJ mol^{-1} made it imperative to heat and cool the sample quickly so as to avoid effects of variations in the temperature on the diffusion profile. At the same time, however, fast cooling below 100 °C was restricted by the need to prevent condensation in the apparatus, and the heating rate likewise slow due to the low exchange temperatures: The effect of convective heat transfer is smaller at lower temperatures. These factors will contribute to deviations from perfect

Fickian diffusion profiles and thereby to the uncertainty in the extracted tracer diffusion coefficients.

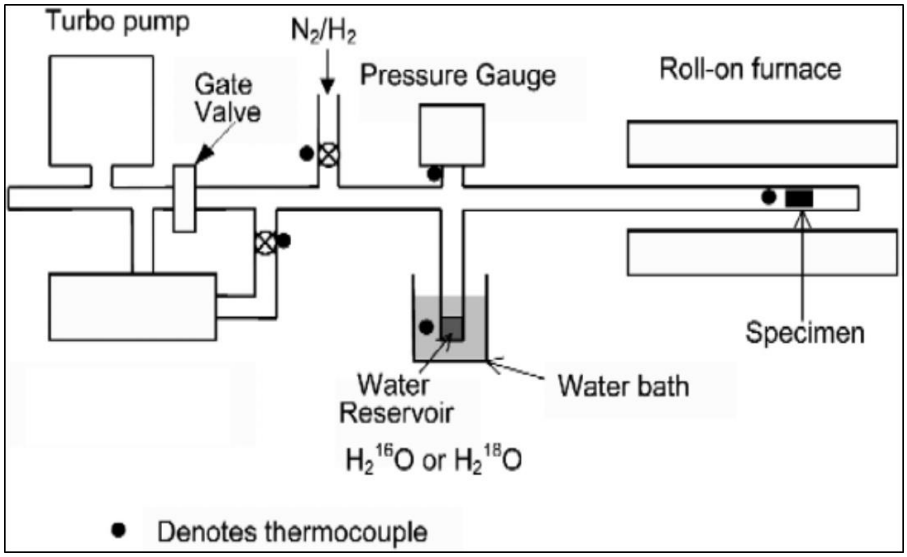

Fig. 3.1: Schematic of isotopic exchange apparatus, by Atkinson et al. [23]. D_2O was used in addition to $H_2{}^{16}O$ and $H_2{}^{18}O$ in the water reservoir.

3.1.2. ToF-SIMS instrumentation

The characterizations described in this study were carried out with a ToF-SIMS machine (ION-TOF GmbH, Münster, Germany), the principle of which was described by De Souza et al. [24]. The main components of the instrument are schematically illustrated in Fig. 3.2 [24]: The Bi^+ Liquid Metal Ion Gun (LMIG) is used to generate secondary ions for analysis, while the second ion gun is used exclusively for sputter removal of sample material. It is a dual source column with a Cs^+ thermal ionization source and an electron impact source for producing $O_2{}^+$ beams. Depth profiling and imaging are accomplished by interlacing the timing cycles of the analysis and sputtering ion beams. Charge compensation during ion bombardment of poorly conducting samples is achieved by flooding the sample surface with ~20 eV electrons. The generated secondary ions are extracted perpendicular to the sample surface and enter the drift tube. Here, ions of a given mass/charge ratio are separated according to their velocity, and the reflectron, an electrostatic mirror, makes sure that ions of the same mass but different velocities arrive at the detector at the same time. Here they are counted and have their arrival time recorded. In this way a complete mass spectrum is acquired for every scan.

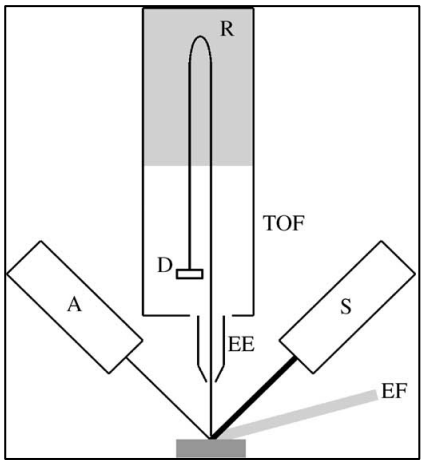

Fig. 3.2: Schematic of a ToF-SIMS IV machine, depicting the main components, by De Souza et al. [24]: two ion guns, a Bi^+ LMIG for analysis (A) and a low-energy gun for sputtering (S); extraction electrode (EE); Time-of-Flight Mass Spectrometer (ToF) with reflectron (R); detector (D); and an electron flood gun (EF).

3.1.3. Analysis mode – imaging and depth profiling

Samples with diffusion profiles extending more than 1 μm were analysed by imaging. The specimens were prepared for imaging by sectioning normal to the surfaces, yielding cross sections parallel to the diffusion direction which were polished to a finish of 1/4 μm. In order to avoid distortions of the ion beam's electric field close to the sample edge, two pieces of the sectioned specimen were mounted together ''head-to-head'', effectively eliminating this edge effect. A sample mounted in this manner is shown after the ToF-SIMS characterizations in Fig. 3.3 (left). A crater of 500 × 500 μm produced by the Cs^+ source is visible, and the area analysed by the Bi^+ LMIG was 100 × 100 μm and positioned in the centre of the sputter area. Each plane in the analysis area was a matrix of 256 × 256 pixels. By summing each column of the matrix parallel to the surface, we obtained line scans perpendicular to the original sample surface. This is shown for OD^- secondary ions in Fig. 3.3 (right), which demonstrates that two line scans may be obtained from a single measurement by conducting the analysis across two sample sections. Furthermore, these line scans pinpoint the relatively few OD^- counts obtainable. In order to improve the quality of the profile, the signals were further manipulated by combining 4 × 4 pixels and thereby produce – at the expense of some spatial resolution – a signal of higher intensity and less scatter. The resulting profiles, after normalization, are those employed in Manuscript IV.

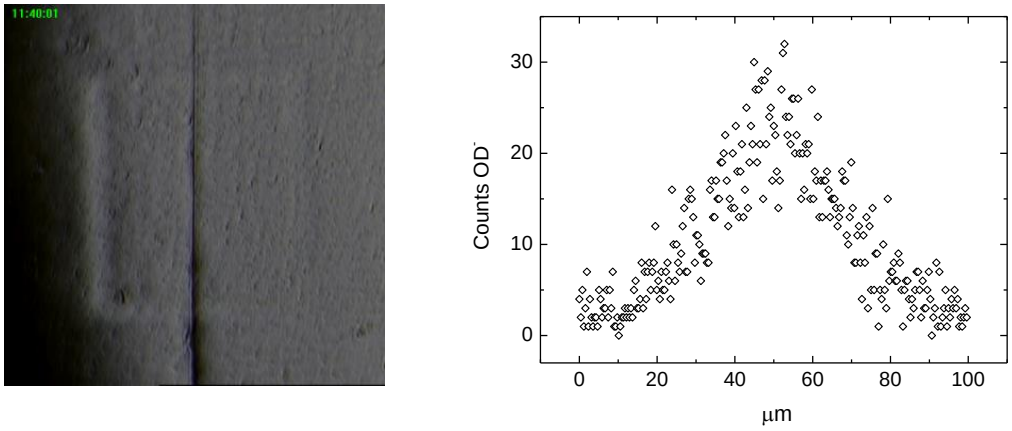

Fig. 3.3: Image of two LWO56 pieces mounted for imaging (left). The visible sputter crater is 500 × 500 µm whereas the analysis area is 100 × 100 µm. Right: the two mirrored line scans of OD^- secondary ions after vertical summation of the measurement array.

Diffusion profiles shorter than ~1 µm were analysed by depth profiling, where the diffusion profile was collected normal to the surface. The crater depth was subsequently measured using a white light interferometer (Zygo New View 200). The Zygo is a general purpose surface profiler that measures the topography of surfaces in three dimensions. Fig. 3.4 shows Zygo micrographs of a crater in a LWO56 specimen after depth profiling. The average crater depth is 439 ± 42 nm.

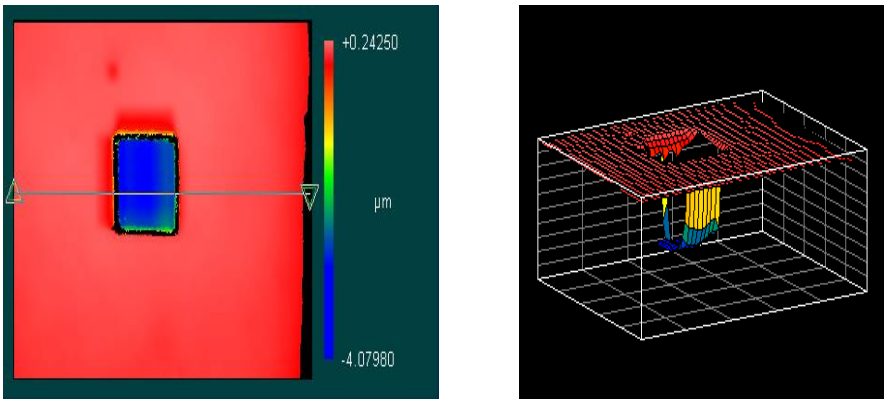

Fig 3.4: White-light interferometer (Zygo New View 200) images of a sputtered crater after depth profiling on a LWO56 sample. The average depth of the crater is 439 ± 42 nm.

3.2. Thermogravimetry

Papers I, II and IV make use of thermogravimetric (TG) measurements to determine hydration and isotope exchange properties of LWO and BCO. A more detailed description of the instruments used is given in the following.

A Netzsch STA (Simultaneous Thermal Analyzer) 449 F1 Jupiter was employed for the TG measurements. This thermobalance takes a sample load of approximately 5 g and has a digital resolution of 0.025 µg. The instrument's interior is sketched in Fig. 3.5 [25]. It is a top-loading, vacuum tight system with a built-in gas supply unit with three mass flow controllers (MFC) for purge and protective gases. The furnace handles up to 1500 °C. In order to protect the balance system, the instrument can take only 2 % water vapour in the gas mixture, achieved by diluting a purge gas containing 2.5 % water vapour (passing through saturated KBr (aq)) with a dry protective gas (passed over P_2O_5 (s)) which is directed through the balance system. The sample holders were slip-on crucibles and plates of alumina, and background measurements were made with empty sample holders to correct for buoyancy and drift.

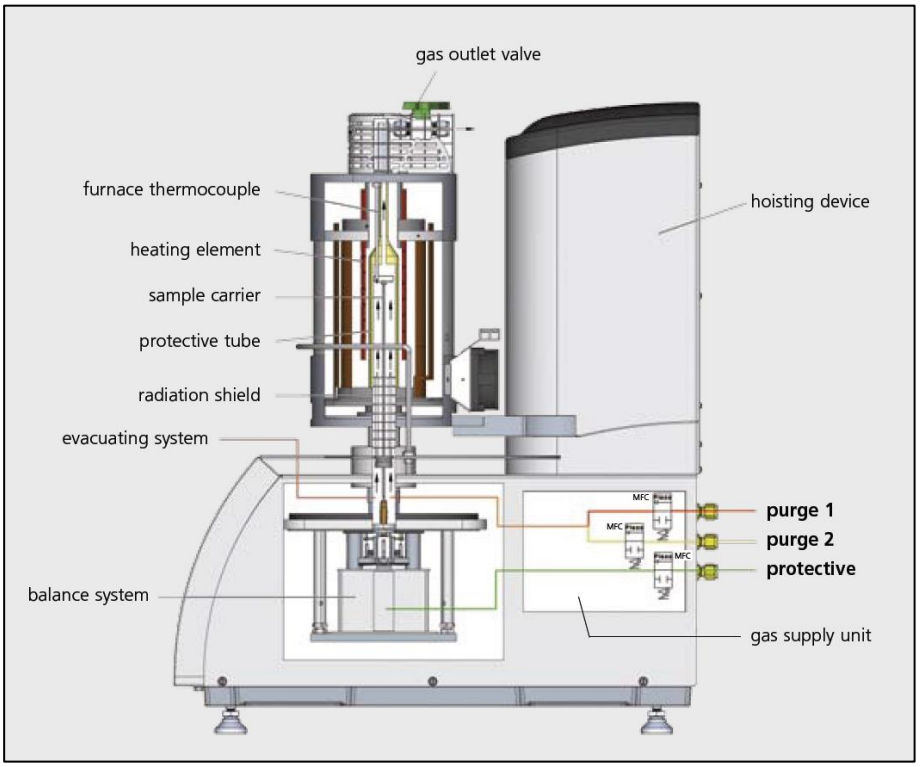

Fig. 3.5: Schematic of the TG (STA 449 F1 Jupiter) [25] with three mass flow controllers.

In Manuscript II a combination of TG and differential scanning calorimetry (TG-DSC) was employed to determine the hydration enthalpy of LWO. The instrument used was a Netzsch STA 449 C Jupiter. The instrument was especially designed to operate under high water vapour pressures, achieved by an external water vapour generator and a special furnace constructed for high water vapour pressures, the latter shown in Fig. 3.6 [26]. The external generator produces 100 % water vapour in a device where the liquid water is completely evaporated at 180 °C. The vapour is introduced into the furnace by a heated transfer line and heating jacket, thereby preventing condensation. The gas lines inside the furnace enable preheating of the vapour inside the outer flow chamber and feed the vapour from the top over the sample. When a second gas is used to dilute the water vapour, this is introduced using the purge gas channel, controlled by a mass flow controller. This purge gas is not shown in Fig. 3.6, but was introduced before the heating collar, close to the water vapour inlet. Pt-Rh crucibles which can take a sample load of approximately 200 mg were employed. Background measurements were made with empty sample- and reference crucibles to correct for the buoyancy occurring during the switch from N_2 (g) to H_2O (g), and for the difference in heat conductivity between the two gases.

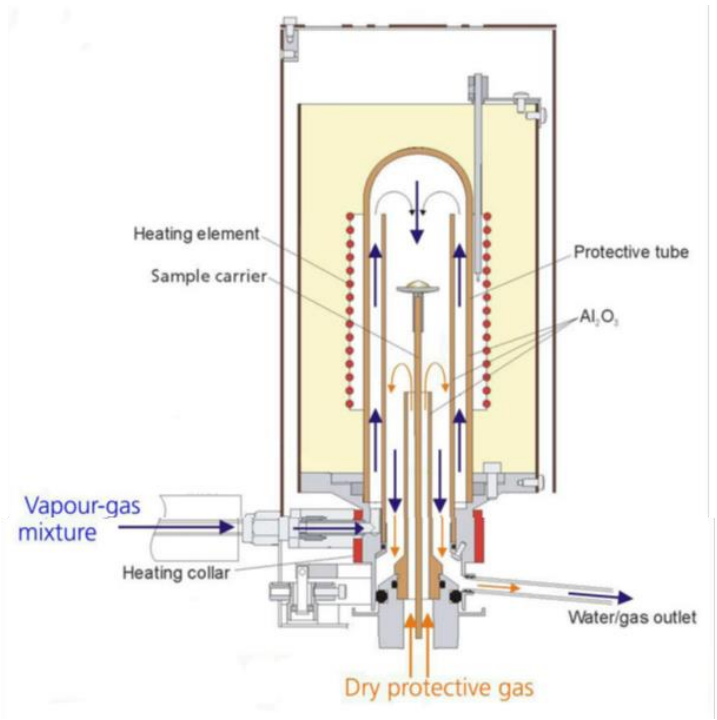

Fig. 3.6: Schematic of the TG-DSC (STA 449 C Jupiter) with water vapour furnace [26].

3.3. Conductivity relaxation measurements

In Manuscript IV we reported on tracer diffusion coefficients of protons obtained by conductivity relaxation measurements of H_2O/D_2O exchange. In the following, some experimental details and a more comprehensive record of the results are given.

The LWO samples were mounted in a measurement cell (Probostat, NorECs, Norway) placed in a vertically positioned tubular furnace. The electrical properties of the samples were investigated by connecting four platinum wires in pairs to two porous platinum electrodes that were attached on the LWO samples. The measurement cell was connected to a gas mixer where the gas flow is directed into the cell by flowmeters with adjustable valves and floating balls. The gas is blown directly onto the electrodes on both sides of the specimen via the outer and inner gas tubes. The normalized conductivity relaxation profiles of LWO recorded after shifts from H_2O to D_2O at 350, 400 and 450 °C are plotted in Fig. 3.7 (left), together with the best fit to the full solution of Fick's second law, as given in Eq. (2.18). The extracted tracer diffusion coefficients and tracer surface exchange coefficients are displayed as a function of reciprocal temperature in Fig. 3.7 (right), compared to the corresponding coefficients as obtained from transient TG measurements.

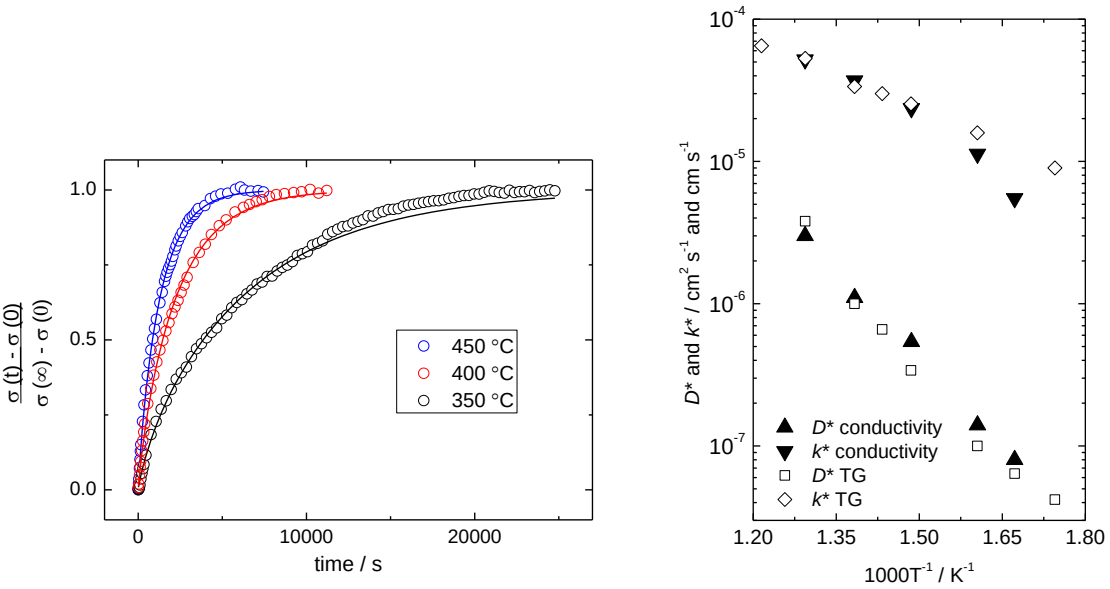

Fig. 3.7: Normalized conductivity relaxation curves of LWO recorded at various temperatures. Open symbols represent experimental data and solid lines the best fit (left). Tracer diffusion coefficients and surface exchange coefficients from conductivity and mass relaxation measurements (right).

3.4. Gas phase analysis with mass spectrometry

The overall methodology of the gas phase analysis with mass spectrometry (GPA-MS) is thoroughly described in Manuscript V, but a more detailed description of the experimental setup and a sketch thereof are included in the following.

Fig. 3.8 shows a schematic illustration made by Anghel et al. [27] of the experimental assembly, originally designed by Hultquist et al. [28, 29], which was used to determine the hydrogen isotope exchange rates in Manuscript V. The reaction tube (60 ml) was made of quartz, whereas the other parts were made of stainless steel. The slab samples were placed inside the reaction tube, which was then heated by a mobile, horizontal tube furnace. The temperature was monitored and controlled with a type S thermocouple. The reaction tube may be evacuated by a roughing pump and supplied with H_2, D_2 or a mixture of the two isotopes from the gas handling system. The pressure and composition of the gas were measured as a function of time by a Pfeiffer CMR 26 pressure gauge (1-1000 mbar) and a Quadrupole MS (Balzers, Prisma 200), respectively. The MS was operated with the channeltron detector and had a practical detection limit of 100 ppm.

Prior to each measurement, the specimen was heated to the reaction temperature and equilibrated in a 1:1 mixture of H_2 and D_2 with a total pressure of 20 mbar, whereupon the chamber was evacuated and the same gas mixture was fed to the reaction tube until 20 mbar. Measurements were performed under both dry (bottle dry) and wet conditions, and the latter had a water vapour content of ~10 % (1:1 mixture of H_2O and D_2O). Wet gases were obtained by placing a beaker with the water mixture inside a stainless steel container in the gas handling system and by pumping this volume down until an atmosphere determined entirely by the vapour pressure of water was obtained. The container was subsequently filled with H_2/D_2 up to the desired total pressure.

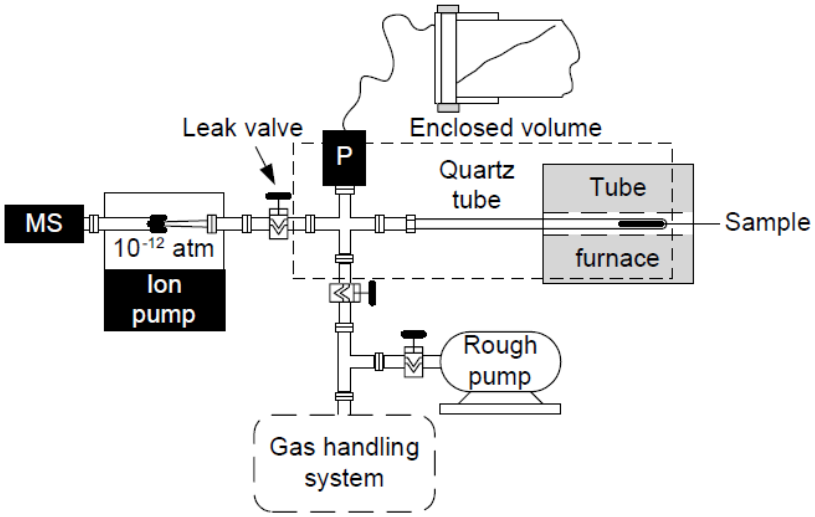

Fig. 3.8: An experimental assembly, schematized by Anghel et al. [27], equivalent to the one used in the GPA-MS measurements.

4. Manuscripts

I **Thermogravimetric relaxation study of the proton conductor lanthanum tungstate, $La_{28-x}W_{4+x}O_{54+d}v_{2-d}$, x = 0.85**

R. Hancke, Z. Li and R. Haugsrud

International Journal of Hydrogen Energy, 37 (2012) 8043-8050

II **Hydration of lanthanum tungstate (La/W = 5.6 and 5.3) studied by TG and simultaneous TG-DSC**

R. Hancke, A. Magrasó, T. Norby and R. Haugsrud

Solid State Ionics, 231 (2013) 25-29

III **The kinetics of hydration and H/D isotope exchange of Y-doped barium cerate and lanthanum tungstate studied by transient thermograviemtry**

R. Hancke, Z. Li and R. Haugsrud

Journal of The Electrochemical Society, 160 (2013) F757-F763

IV **Determination of proton- and oxide ion tracer diffusion in lanthanum tungstate (La/W=5.6) by means of ToF-SIMS**

R. Hancke, S. Fearn, J. Kilner and R. Haugsrud

Physical Chemistry Chemical Physics, 14 (2012) 13971-13978

V **Hydrogen surface exchange on proton conducting oxides studied by gas phase analysis with mass spectrometry**

R. Hancke, Z. Li and R. Haugsrud

Journal of Membrane Science, 439 (2013) 68-77

Manuscript I

Thermogravimetric relaxation study of the proton conductor lanthanum tungstate, $La_{28-x}W_{4+x}O_{54+d}v_{2-d}$, x = 0.85

R. Hancke, Z. Li and R. Haugsrud

International Journal of Hydrogen Energy, 37 (2012) 8043-8050

Manuscript II

Hydration of lanthanum tungstate (La/W = 5.6 and 5.3) studied by TG and simultaneous TG-DSC

R. Hancke, A. Magrasó, T. Norby and R. Haugsrud

Solid State Ionics, 231 (2013) 25-29

Manuscript III

The kinetics of hydration and H/D isotope exchange of Y-doped barium cerate and lanthanum tungstate studied by transient thermograviemtry

R. Hancke, Z. Li and R. Haugsrud

Journal of The Electrochemical Society, 160 (2013) F757-F763

Manuscript IV

Determination of proton- and oxide ion tracer diffusion in lanthanum tungstate (La/W=5.6) by means of ToF-SIMS

R. Hancke, S. Fearn, J. Kilner and R. Haugsrud

Physical Chemistry Chemical Physics, 14 (2012) 13971 – 13978

Manuscript V

Hydrogen surface exchange on proton conducting oxides studied by gas phase analysis with mass spectrometry

R. Hancke, Z. Li and R. Haugsrud

Journal of Membrane Science, 439 (2013) 68-77

5. Summarizing discussion

This chapter is devoted to a discussion of the most central findings in the five manuscripts. The manuscripts are treated collectively, thus allowing introduction of new perspectives which were not foreseeable or practical to include within the limited framework of each individual paper. Treating all the manuscripts as a whole, this section also opens up for a discussion of experimental and analytical possibilities and limitations, and, moreover, offers some thoughts on the general challenges one faces when seeking to characterize and optimize kinetic properties of HTPCs.

5.1. Bulk transport

5.1.1. Transient H/D isotope exchange – applicability and limitations

Manuscript I, III and IV show that within the uncertainty imposed by kinetic isotope effects, the self-diffusivity of protons, $D_{\mathrm{OH}_{\mathrm{O}}^{\bullet}}$, and the associated enthalpy of mobility, ΔH_{mob}, may be determined directly from H/D isotope exchange by transient thermogravimetry (TG) and conductivity measurements, and from profiling with time-of-flight secondary ion mass spectrometry (ToF-SIMS). The immediate attraction of these techniques is that one does not have to make use of the assumptions and simplification behind a defect chemical model. However, certain restrictions have been demonstrated to apply: In Manuscript II we rationalize that isotope exchange experiments performed under conditions where a material is not fully hydrated will be accompanied by simultaneous in- or out-diffusion of a small amount of water due to the different vapour pressures and hydration thermodynamics of H_2O and D_2O [30]. For LWO, the extracted diffusion coefficients consequently do not represent pure tracer diffusion of protons, and the activation energy determined from Arrhenius plots will contain a contribution from the enthalpy of mobility of oxygen vacancies and enthalpy of hydration. This is depicted in Fig. 5.1, where the diffusivity (left y-axis) and concentration (right y-axis) of protons in LWO56 is plotted as a function of reciprocal temperature. Dotted lines are included as visual aids to pinpoint that an increase in the temperature dependence takes place essentially at the same temperature where the material starts to dehydrate, thus shifting from an activation energy solely representing the

enthalpy of mobility of protons (~65 kJ mol^{-1}), to one influenced by the diffusivity of oxygen vacancies and hydration thermodynamics as well.

Thus, prior knowledge of the material's hydration thermodynamics is, after all, necessary in order to choose the appropriate conditions for determining the enthalpy of mobility of protons. Nonetheless, when familiar with these restrictions, transient isotope exchange experiment is a convenient and reliable means of obtaining fundamental transport properties of a proton conductor.

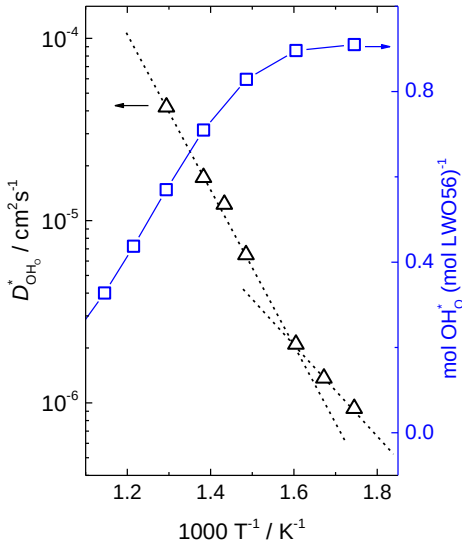

Fig. 5.1: Tracer diffusion coefficient of protons (left y-axis) and concentration of protons (right y-axis) vs. reciprocal temperature for LWO56. The activation energy increases essentially at the same temperature where the material starts dehydrating.

5.1.2. Oxygen tracer diffusion – influence of vacancy ordering

In Manuscript IV, the oxygen tracer diffusion coefficient (D_O^*) of LWO56 was determined from quenched ^{18}O tracer profiles by ToF-SIMS. These properties could in principle have been extracted from TG relaxation measurements as well, but due to the cost of water enriched in ^{18}O and the lack of experimental setups permitting recovery of the isotope, these experiments were not performed. From D_O^*, the diffusivity of oxygen vacancies, $D_{v_O^{\bullet\bullet}}$ was calculated. The associated apparent activation enthalpy of 142 kJ mol^{-1} is significantly higher than the enthalpy of 85 kJ mol^{-1} estimated from conductivity measurements [10]. Since the isotope exchange was confined to lower temperatures (below 650 vs. 1100 °C), it

was suggested that the value extracted from isotope annealing contains a contribution from oxygen vacancy ordering. Admittedly, the ToF-SIMS study could have encompassed a larger number of oxygen tracer exchange measurements over a larger temperature span to discern whether the Arrhenius plot actually had a convex shape, typical for defect association processes. This would allow fitting of the data to a model taking the energy contribution of oxygen vacancy ordering into account. Nevertheless, other studies also indicate that oxygen vacancies cluster in the La-richer compositions of LWO: In Manuscript II it was found that whereas LWO53 hydrated 100 % according to the applied defect chemical model, only 66 % of the predicted oxygen vacancies in LWO56 were hydrated. We speculated that this deviation from full hydration could be due to either segregation of a small amount of La_2O_3 or ordering of the oxygen vacancies, - being more plentiful in LWO56 than in LWO53. Furthermore, in a separate study by Magrasó et al. [31] employing transmission electron microscopy (TEM), LWO53 showed evidence of diffuse scattering from oxygen vacancy disorder (Fig 5.2 a), whereas LWO57, with the higher concentration of vacancies, did not (Fig 5.2 b). This was interpreted as being due to a certain degree of oxygen vacancy ordering in LWO57.

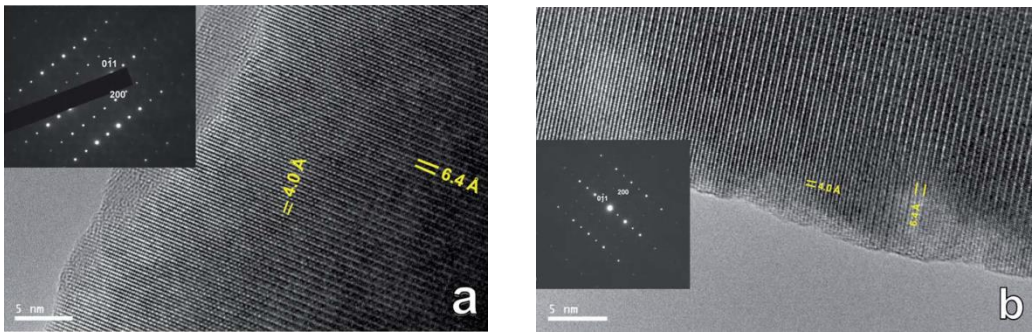

Fig 5.2: TEM micrographs and the corresponding electron diffraction patterns showing a view down the [011] zone axis for (a) LWO53 and (b) LWO57 [31]. Diffuse scattering can be detected in the W-richer composition (a).

5.1.3. Chemical diffusion – determination of hydration mechanism

Conductivity relaxation measurements performed by inducing step changes in the water vapour pressure can in many cases differentiate between one-fold and two-fold hydration processes. Mass relaxation measurements, on the other hand, yield less clear information in this respect; in-diffusion of both protons and oxide ions yield monotonic increases in weight

whether they are coupled or separate. This is discussed in Manuscript III. In Manuscript IV we, furthermore, show that ion exchange followed by ToF-SIMS analyses in fact offer an alternative way of obtaining information about the hydration mechanism because it allows for separate analysis of the individual species' diffusion front: By annealing a nominally dry LWO56 sample in $D_2{}^{16}O$ we could follow the deuterium diffusion front and, by comparing to the tracer diffusion front, demonstrate how the slow oxide ions retard the diffusion of protons across the material. Fast independent diffusion of hydrogen was thereby excluded. An experiment which would be even more instructive in this respect is isotopic labelling of both hydrogen and oxygen by hydrating the sample in $D_2{}^{18}O$, enabling analyses of the hydrogen- and oxygen diffusion profiles *simultaneously*.

5.2. Surface exchange reaction

In the following, some of the premises and background for the treatment of empirical surface exchange coefficients are emphasized and discussed.

As discussed in Manuscript III and V, it may be advantageous to differentiate between the overall electroneutrality condition applying to the oxides under hydration (*i.e.* protons consuming oxygen vacancies as described in Eq. (2.1)), and the partial reactions constituting this total acid-base reaction. The two-fold hydration mechanism comprises a good example, in which the hydration reaction is decomposed into a reduction and an oxidation reaction. Thus, even though very few oxides dissolve protons from H_2 (g) with electrons as charge compensating defects – *n*-type ZnO comprising a famous exception [32] – redox reactions may play a vital role on a local scale, and should particularly be considered when the surface exchange reaction is under separate scrutiny.

A similar distinction between surface redox and acid-base reactions is gradually being recognized with respect to oxide ion conductors. Up until recently, the research activity on surface exchange mechanisms of this class of materials was exclusively concerned with the oxide surface's interaction with molecular oxygen. Studies have, however, shown that the surface exchange rate for a number of materials increases significantly when water vapour is present in the ambient, see *e.g.* [33-36]. This finding has raised consciousness about the importance of controlling the pH_2O during exchange anneals, and one might find that it sheds light on conflicting results in literature. Perhaps the proton conduction community,

which has a stronger tradition of controlling the water vapour pressure during experiments, is even better equipped to meet this analytical challenge.

In the analysis and discussion of surface exchange mechanisms for LWO, LWMO and BCO in Manuscript III and V, a crude division between a surface exchange reaction with water (analyzed with TG) and a reaction with molecular hydrogen (analyzed with MS) has been made. It is important to note that this differentiation was made to provide a starting point, and that the two reactions may very well be connected in a sequence more complex than those outlined therein. An oversimplification of the kinetic landscape may explain why the analyses do not always account for the results in all contexts. By way of example, we argue in Manuscript I and III that under reducing conditions, the chemical surface exchange coefficient of LWO (k^{δ}_{red}), recorded upon a step change in the partial pressure of hydrogen and water, must be dominated by a redox reaction with hydrogen. This rationalization is based on the change in activation energy under reducing conditions and the effect of platinum coating. In Manuscript V, on the other hand, we explicitly measure the same material's activity towards H_2 dissociation and exchange by gas phase analysis with mass spectrometry (GPA-MS), expressed by the surface exchange coefficient k_s. When comparing the activation energy of k_s (~130 kJ mol^{-1}) and k^{δ}_{red} (~25 kJ mol^{-1}), however, it is clear that these surface exchange coefficients must represent two different rate determining steps.

One might find the answer to this difference in the fact that the TG experiments yielding k^{δ}_{red} necessarily involve exchange with bulk protons (so-called hetero molecular exchange), whereas the process represented by k_s actually may take place only by homo molecular exchange. Smith et al. [37] designed the GPA-MS experiments in a manner which enabled differentiation between these two principal reaction mechanisms. They measured the oxygen exchange on a number of oxides by the same GPA-MS technique as us (see Chapter 3.4), except that the materials were pre-equilibrated in a single isotope ($^{16}O_2$) instead of a 50:50 mixture of $^{16}O_2$ and $^{18}O_2$ such as we did with H_2 and D_2. Typical results are presented in Fig. 5.3 [37] below. Here, the concentration of $^{16}O_2$ (○) is seen to increase over time for both experiments, which is taken as an evidence of hetero molecular exchange. Furthermore, by a comparison of the equilibration rates of $^{16}O/^{18}O$ and $^{16}O_2/^{16}O^{18}O/^{18}O_2$, the authors argue that qualitative information about the rate limiting exchange mechanism is obtainable: When the equilibration rates are identical, as in the left figure, exchange with bulk oxygen is probably the bottleneck of the reaction, whereas when the equilibration rates

of the atomic species are faster than that of the molecules (right), the exchange mechanism may be limited by dissociation or charge transfer.

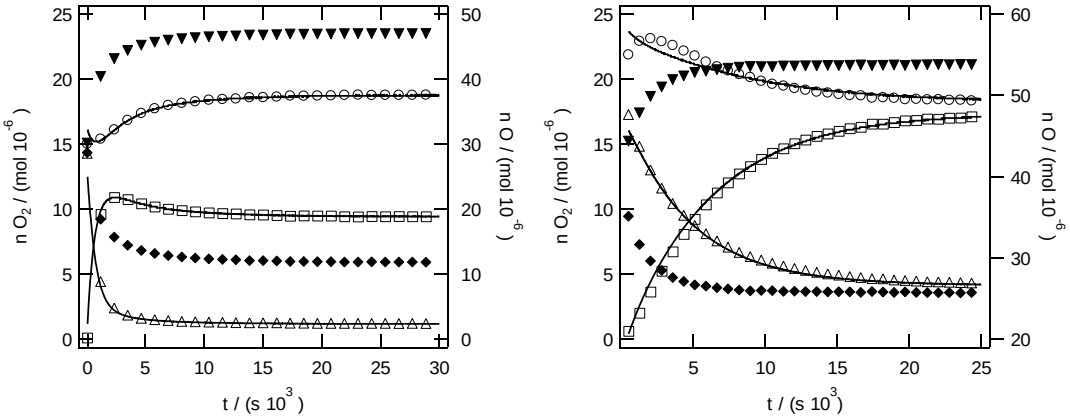

Fig. 5.3: Time evolution of the isotopic composition of the atmosphere over $La_{0.9}Sr_{0.1}FeO_3$ (left) and La_2NiO_4 (right), by Smith [37]. The left and right axes show the composition with respect to molecular species and isotopic atoms, respectively. Solid curves represent simulations, and markers represent the measurements; $^{16}O_2$ (○), $^{16}O^{18}O$ (□), $^{18}O_2$ (Δ), ^{16}O (▼) and ^{18}O (♦).

5.3. Relation between bulk diffusion and surface exchange rates

5.3.1. Critical thickness – theory and practice

In Manuscript V we estimated the critical thicknesses of different HTPCs based on their ambipolar conductivities and H_2-D_2 surface exchange rates according to Eq. (2.23). In the following, these estimates are compared with the results of flux measurements.

Recently, Gil et al. [38] published results of hydrogen flux measurements on supported membranes of LWO56 with thicknesses of 25-30 μm. Employing a feed gas of wet 10 % H_2 in Ar, they obtained an area specific flux of about 0.07 mL min^{-1} cm^{-2} at 900 °C. Erdal et al. [39] have earlier performed corresponding flux measurements on a LWO56 disk specimen in which the permeation rate was assumed to be limited by bulk diffusion. Extrapolation of their results predicts that a 30 μm thick membrane will yield an area specific flux of ~0.08 mL min^{-1} cm^{-2} under the same conditions. The excellent agreement with the results obtained by Gil et al. indicates that the permeation rates of the thin membranes indeed were limited

by bulk diffusion and that the critical thickness of LWO56 is less than 30 μm at 900 °C. In our calculations, L_C was found to be about 10 μm at the same temperature; a result which, thus, remains uncontested by the flux measurements.

For molybdenum-substituted lanthanum tungstate (denoted LWMO in Manuscript V), we calculated that L_C would reach 30 μm at 800 °C. Unpublished permeation measurements on the same composition performed by Protia A/S at 800 °C show that the permeability of a 25 μm thick membrane is smaller than that of an 80 μm thick membrane. The former permeability is, however, enhanced to the same level as that of the 80 μm thick sample upon platinum coating on the surface. These results indicate that the critical thickness of LWMO is between 25 and 80 μm at 800 °C and that our estimate of L_C is thus within the correct range.

L_C of 5 mol-% Yb-doped $SrCeO_3$ (SCO) was in our calculations found to decrease with increasing temperature and become as small as 0.02 μm at 800 °C. Hamakawa et al. [40] earlier showed that the hydrogen flux of this material remains inversely proportional to the thickness of the membrane even at a thickness of 2 μm, which – if not verifying our results – at least confirms that the critical thickness is smaller than for the other materials considered. For Y-doped $BaCeO_3$ (BCO), the critical thickness reaches more than 200 μm at 800 °C. However, this material is generally not considered for membrane applications anyway, unless compositional changes improving the electronic conductivity (and chemical stability) can be made.

A comparison of the performance of these materials shows that SCO exhibits the highest permeation rate: Yoon et al. [41] achieved an area specific flux of 0.6 mL min^{-1} cm^{-2} for a 10 mol-% Eu-doped $SrCeO_3$ membrane of 30 μm thickness at 900 °C under feed compositions of wet H_2 (1 atm), which is a factor of three higher than that for LWO56 under such a large chemical potential gradient in hydrogen (0.2 mL min^{-1} cm^{-2} as estimated by Erdal et al. [39]). For LWMO, the preliminary results reported by Protia A/S show an area specific flux of 0.06 mL min^{-1} cm^{-2} for the 25 μm thick membrane, recorded under feed compositions of wet 10 % H_2 at 900 °C.

5.3.2. Calculating critical thickness – assumptions and limitations

When comparing calculated critical thicknesses to those determined experimentally from hydrogen flux measurements, it should be noted that L_C is calculated under the assumption

of identical surface kinetics on both sides of the membrane. This assumption may, however, be flawed as the permeate side is exposed to a gas with higher pO_2 and lower pH_2O than the feed side. Take for example LWO, whose surface exchange rate based on our GPA-MS measurements has been suggested to be limited by charge transfer: Due to the higher pO_2 and hence lower concentration of electronic charge carriers, LWO will exhibit a slower exchange rate on the permeate side under operating conditions. If the effect of less reducing sweep side conditions is more pronounced for the surface exchange rate than for the bulk transport rate, this would lead to an underestimated L_C.

Furthermore, taking simply the ratio between D and k (which has the dimension of length) as the critical thickness is, indeed, useful as a guide for choosing the appropriate sample thickness in the design of a transient experiment. This is discussed in the next section. However, as an estimate of actual limitations to hydrogen permeation, one must keep in mind that Eq. (2.23) does really only reduce to $D_{\mathrm{OH}_{\mathrm{O}}^{\bullet}}/k_s$ when $t_{e'} = 1$. Of the materials considered herein, this condition is only fulfilled by LWMO. Thus, when we in Manuscript I refer to the ratio between D and k of LWO (both chemical and tracer coefficients) as a quantity of impact with respect to hydrogen separation technology, this should be considered a first approximation. By calculating L_C in this manner we severely overestimate the ambipolar conductivity of LWO and thereby also overestimate the quantity of L_C itself. As shown in Manuscript V, it will amount to 1500 μm at 800 °C.

In this respect it is also important to be conscious about *which* empirical bulk and surface coefficients one employs when estimating L_C according to the ratio between D and k. For instance, the chemical diffusion coefficient of water is actually rather unfit to express anything about limitations to hydrogen flux unless the relaxation is fully limited by proton transport. Moreover, the appropriate surface exchange coefficient depends on the dominating surface reaction: By way of example, we employ the surface reaction rate for H_2-D_2 exchange as measured in Manuscript V when L_C is estimated according to Eq. (2.23). However, if the incorporation of protons is rather favoured by the reaction with water – which it seems to be for LWO below 800 °C – one may speculate whether it is more suitable to employ the thermogravimetrically derived surface exchange coefficient, k^* (converted to exchange rate) in the expression for L_C. For LWO, this will lead to a smaller critical thickness, *e.g.* by a factor of 5 at 700 °C.

5.3.3. The D/k ratio – importance to experimental design

Ideally, one can extract both surface- and bulk kinetic information from *one* relaxation curve. However, as stressed herein and discussed in literature [42-45], this exercise requires a suitable sample; the smallest dimension of the sample should be close to the ratio between *D* and *k*. And even then, it is difficult to fit both *D* and *k* simultaneously since several pairs of constants can make a decent fit. To exemplify the limitations imposed by sample dimensions, let us compare some of our results to literature: In Manuscript III we found that a 1.3 mm thick BCO sample was limited by bulk transport, and thus that the fit to the relaxation profile was insensitive to k^{δ}. Yashiro et al. [46], on the other hand, extracted both bulk- and surface kinetics from a BCO sample with the dimensions 3 × 5 × 10 mm. They obtained exchange coefficients several orders of magnitude smaller than those we found for a sample with the smallest dimension 0.5 mm. Differences in surface roughness will clearly affect the maximum thickness at which surface kinetics is no longer obtainable, but it nonetheless seems clear that the shape of the conductivity relaxation profile recorded by Yashiro et al. must have been insensitive to the value of k^{δ}.

Finally, I wish to emphasize that the crucial role played by sample dimensions and the ratio between bulk- and surface transport kinetics with respect to the derivation of surface kinetic properties is mainly restricted to the techniques which probe changes in the *material* (*e.g.* TG and ToF-SIMS). For analyses of the gas phase composition, as concerned with in Manuscript V, the obtained exchange rate will, to the best of my understanding, be governed by the surface reaction irrespective of sample dimension. This may be rationalized in the following manner: If bulk equilibrates faster than the surface exchange (typically when the surface-to-volume ratio is large), the surface exchange reaction will clearly be the bottleneck for HD formation from H_2:D_2 gas mixtures. But also, if bulk equilibrates considerably slower than the surface, HD molecules will form on the surface independent of the bulk transport process, and its formation rate will therefore be a measure of the surface exchange rate. In Fig. 5.4 I have plotted the exchange rate, *R*, of LWO56 as a function of reciprocal temperature measured on both a slab (~3 cm^2) and powders (~650 cm^2). The figure suggests that the same rate-determining step of HD formation applies to the powder and to the slab, in support of the reasoning above.

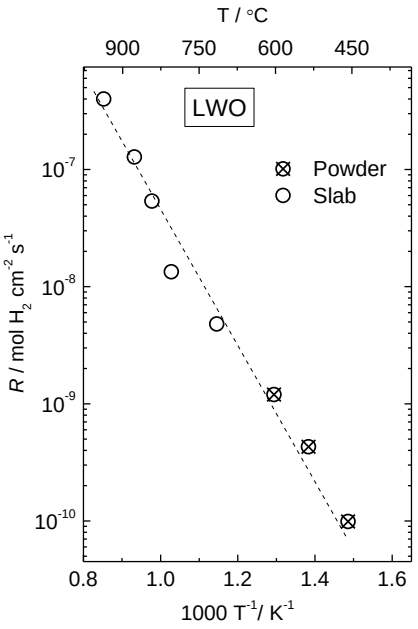

Fig. 5.4: Surface exchange rate on LWO56 vs. 1000/T obtained from a slab sample and from powders. The similar temperature dependencies suggest that GPA-MS exclusively probes the surface exchange rate irrespective of the ratio between surface area and bulk volume.

5.3.4. log k-log D plots

For oxide ion conductors, a linear correlation has been found between the logarithms of oxygen tracer surface exchange coefficients, k_O^*, and diffusion coefficients, D_O^*, which range of validity covers all materials within a given class [47, 48]. This rather reputed correlation plot is shown in Fig. 5.5 (left) [47] for two classes of materials, namely perovskites which are predominantly electronically conducting, and purely ionically conducting fluorites. It is proposed that the correlation between D_O^* and k_O^* depends on the ratio of the ionic to the electronic conductivity, and that it thus indicates which point defect is playing a rate-determining role in the transport process. The k_O^* - D_O^* correlation also implies a linear relationship between the activation energy for surface exchange and the enthalpy for oxygen incorporation, $E_{act,\,k} = b\ E_{act,\,D}$ [49].

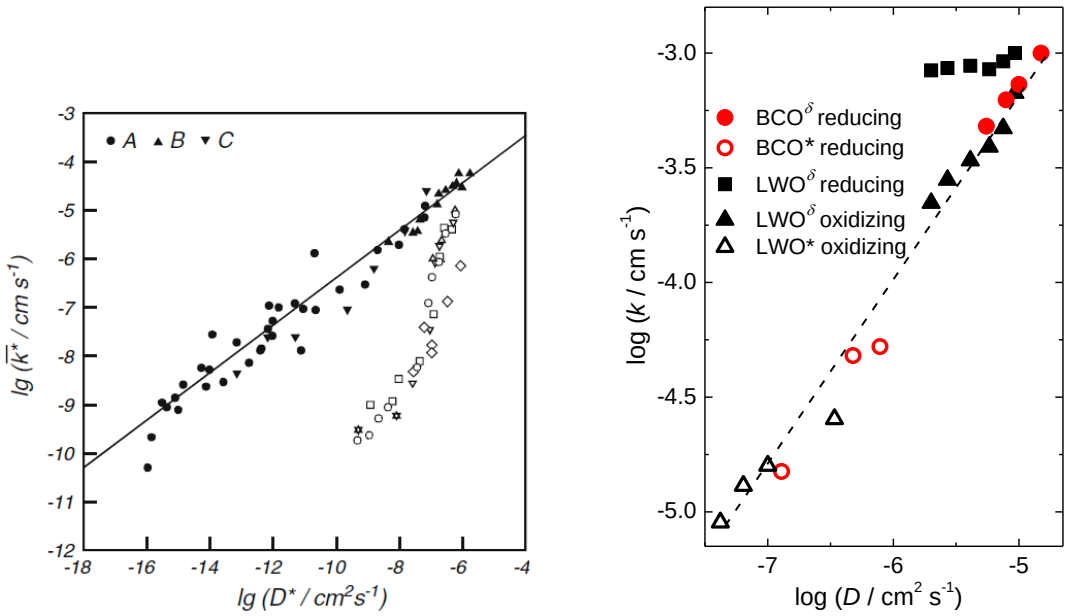

Fig. 5.5 left: Correlation between tracer diffusion coefficients and surface exchange coefficients of ^{18}O exchange for (Ln,Sr)(Mn,Fe,Co)O_3 perovskites (solid symbols) and fluorite electrolytes with minor electronic conductivity (open symbols), by De Souza et al. [47]. Right: Correlation between chemical (δ) and tracer (*) bulk and surface transport coefficients of LWO and BCO recorded under reducing and oxidizing conditions.

In Fig. 5.5 (right) a similar diagram has been constructed for the transport coefficients of BCO (perovskite) and LWO (fluorite-related). Both the chemical and tracer transport coefficients are included (D^{δ}-k^{δ} and D^{*}-k^{*}, respectively) and, except for the chemical transport coefficients of LWO recorded under reducing conditions, the two materials display a similar linear correlation ($E_{act,\,k}$ is between 0.45 and 0.6 $E_{act,\,D}$). It is interesting that the correlation between D^{δ} and k^{δ} constitutes essentially an extension of the tracer correlation plot, despite the variance in activation energy between the different diffusion coefficients and the different surface exchange coefficients (*c.f.* Manuscript III). According to the conclusions drawn with respect to the correlation plot of oxide ion conductors, this suggests that the same point defect limits the surface exchange reaction of LWO (oxidizing conditions) and BCO in both chemical (ΔpH_2O) and tracer (H_2O/D_2O) experiments. This finding corresponds with the results obtained in Manuscript III based on which oxygen vacancies were designated a key role in the limiting exchange mechanism of both LWO and BCO; it was suggested that they acted as sites for incorporation of hydroxide groups, and as catalytic aid in the dissociation of water, respectively. The surface exchange of LWO under

reducing conditions, on the other hand, was proposed limited by a redox reaction involving H_2 (g), hence rationalizing the different slope in the correlation plot.

6. Conclusions

In the present work, bulk transport and surface kinetics of proton conducting oxides are determined by in-situ mass relaxation measurements and ex-situ profiling with ToF-SIMS. Under the appropriate conditions, information about surface exchange and diffusion of protons, oxide ions and water may be obtained. For the relaxation measurements, samples of various dimensions should be employed in order to obtain reliable parameters for both surface- and bulk processes, whereas for the ex-situ profiling measurements, an appropriate ratio between bulk and surface coefficients is necessary to extract both *k* and *D* from the diffusion profile. The present work shows, furthermore, that analyses of the distribution of H-D isotope couples in the gas phase as a function of time by means of mass spectrometry is a suited technique to probe the oxide surfaces' catalytic activity towards hydrogen adsorption and dissociation.

The enthalpy of hydration of lanthanum tungstate ($La_{28-x}W_{4+x}O_{54+3x/2}$, denoted LWO) is approximately -85 kJ mol^{-1} and the enthalpy of mobility of protons 65 kJ mol^{-1}. The activation energy of oxygen tracer diffusion is 176 kJ mol^{-1} between 300 and 650 °C, containing a contribution of the energy associated with oxygen vacancy ordering. LWO hydrates by ambipolar diffusion of protons and oxide ions, and the activation energy of the chemical diffusion coefficient below 700 °C is 120 kJ mol^{-1}. For 10 mol-% Y-doped $BaCeO_3$ (BCO) the diffusivity of protons is about one order of magnitude faster than in LWO, and the enthalpy of mobility of protons is 43 kJ mol^{-1}. The chemical diffusion of water is also faster than in LWO and has an activation energy of 52 kJ mol^{-1}. The reduction and oxidation processes constituting two-fold hydration of BCO under oxidizing conditions cannot easily be separated in a mass relaxation profile.

The chemical and tracer surface exchange coefficients of LWO and BCO recorded by transient thermogravimetry are of similar magnitudes and have activation energies in the range of 25-50 kJ mol^{-1}. For LWO, the activation energy is lower under reducing conditions than under oxidizing. Platinum nano-particles increase the chemical exchange rate at LWO surfaces under reducing conditions, whereas platinum has minimal effect on the surface exchange rate at BCO surfaces. The thermogravimetrically derived surface exchange

coefficients are proportional to approximately $pH_2O^{1/2}$ and pH_2O^0 for BCO and LWO, respectively. The rate of H_2 dissociation and exchange on LWO, measured by gas phase analysis of H_2-D_2 isotope couples, has an activation energy of 130 kJ mol^{-1}, whereas the corresponding exchange rate on a Mo-substituted LWO specimen displays virtually no temperature-dependency. The exchange rate on BCO has an activation energy of ~ 50 kJ mol^{-1}. These exchange rates are essentially independent of water vapour pressure, but exhibit functional proportionalities to the hydrogen pressure ranging from 0.5 to 1.

The lumped surface exchange coefficients obtained by the described techniques are indeed useful for the sake of estimating critical thicknesses, as well as making rationalizations about which rate determining step they represent based on a relation between partial pressure dependencies and the materials' point defect structure. Our results show, by way of example, that surface modifications of lanthanum tungstates are necessary to fully exploit the potential thin membranes offer with respect to hydrogen flux. We, furthermore, propose that the exchange rate of water at the surface of lanthanum tungstate is limited by incorporation of hydroxide groups, whereas the H_2-D_2 exchange reaction is limited by adsorption and partial oxidation of hydrogen molecules. For a full deconstruction of the various surface exchange reactions into a set of elementary steps, however, future studies should endeavour more control over the oxide surfaces, even on an atomistic scale. More thorough investigations of surface structures, compositions and effects of surface modifications should thus be made, and specimens with more defined surfaces (*e.g.* single crystals) employed.

References for Chapters 1-3 and 5

[1] T. Takahashi, H. Iwahara, Solid-state ionics: protonic conduction in perovskite type oxide solid solutions, Revue de Chimie Minerale, 17 (1980) 243-253.

[2] N. Bonanos, B. Ellis, K.S. Knight, M.N. Mahmood, Ionic conductivity of gadolinium-doped barium cerate perovskites, Solid State Ionics, 35 (1989) 179-188.

[3] H. Iwahara, T. Esaka, H. Uchida, N. Maeda, Proton conduction in sintered oxides and its application to steam electrolysis for hydrogen production, Solid State Ionics, 3-4 (1981) 359-363.

[4] K.D. Kreuer, E. Schoenherr, J. Maier, Proton and oxygen diffusion in $BaCeO_3$ based compounds: A combined thermal gravimetric analysis and conductivity study, Solid State Ionics, 70-71 (1994) 278-284.

[5] P.I. Dahl, R. Haugsrud, H.L. Lein, T. Grande, T. Norby, M.-A. Einarsrud, Synthesis, densification and electrical properties of strontium cerate ceramics, Journal of the European Ceramic Society, 27 (2007) 4461-4471.

[6] S. Hamakawa, T. Hibino, H. Iwahara, Electrochemical hydrogen permeation in a proton-hole mixed conductor and its application to a membrane reactor, Journal of the Electrochemical Society, 141 (1994) 1720-1725.

[7] H. Matsumoto, F. Asakura, K. Takeuchi, H. Iwahara, Transient phenomena of an electrochemical hydrogen pump using a $SrCeO_3$-based proton conductor, Solid State Ionics, 129 (2000) 209-218.

[8] T. Scherban, A.S. Nowick, Bulk protonic conduction in ytterbium doped strontium cerium oxide ($SrCeO_3$), Solid State Ionics, 35 (1989) 189-194.

[9] S.J. Song, E.D. Wachsman, J. Rhodes, S.E. Dorris, U. Balachandran, Numerical modeling of hydrogen permeation in chemical potential gradients, Solid State Ionics, 164 (2003) 107-116.

[10] S. Erdal, L.-E. Kalland, R. Hancke, J. Polfus, R. Haugsrud, T. Norby, A. Magrasó, Defect structure and its nomenclature for mixed conducting lanthanum tungstates $La_{28-x}W_{4+x}O_{54+3x/2}$, International Journal of Hydrogen Energy, 37 (2012) 8051-8055.

[11] R. Haugsrud, Defects and transport properties in Ln_6WO_{12} (Ln=La, Nd, Gd, Er), Solid State Ionics, 178 (2007) 555-560.

[12] Protia, PCT/EP2011/051970, (2011).

[13] A. Magraso, C. Frontera, D. Marrero-Lopez, P. Nunez, New crystal structure and characterization of lanthanum tungstate "La_6WO_{12}" prepared by freeze-drying synthesis, Dalton Transactions, (2009) 10273-10283.

[14] C. Solis, S. Escolastico, R. Haugsrud, J.M. Serra, $La_{5.5}WO_{12-d}$ Characterization of Transport Properties under Oxidizing Conditions: A Conductivity Relaxation Study, Journal of Physical Chemistry C, 115 (2011) 11124-11131.

[15] M. Yoshimura, J.F. Baumard, Electrical conductivity of solid solutions in the system cerium oxide-lanthanum tungsten oxide (CeO_2-La_6WO_{12}), Materials Research Bulletin, 10 (1975) 983-988.

[16] A.S. Nowick, A.V. Vaysleyb, Isotope effect and proton hopping in high-temperature protonic conductors, Solid State Ionics, 97 (1997) 17-26.

[17] J. Maier, Physical Chemistry of Ionic Materials: Ions and Electrons in Solids, John Wiley & Sons, Ltd, Chichester, 2004.

[18] H. Yu Ji, J.-S. Lee, J. Maier, Peculiar nonmonotonic water incorporation in oxides detected by local in situ optical absorption spectroscopy, Angewandte Chemie (International ed. in English), 46 (2007) 8992-8994.

[19] J. Crank, The Mathematics of Diffusion, 2d ed., Oxford University Press, Oxford, 1975.

[20] H.J.M. Bouwmeester, A.J. Burggraaf, Dense ceramic membranes for oxygen separation, CRC Handb. Solid State Electrochem., (1997) 481-553.

[21] M. Leonhardt, J. Jamnik, J. Maier, In situ monitoring and quantitative analysis of oxygen diffusion through Schottky-barriers in $SrTiO_3$ bicrystals, Electrochemical and Solid-State Letters, 2 (1999) 333-335.

[22] E. Hörnlund, Studies of dissociation of diatomic molecules with isotope spectroscopy, Applied Surface Science, 199 (2002) 195-210.

[23] A. Atkinson, R.J. Chater, R. Rudkin, Oxygen diffusion and surface exchange in $La_{0.8}Sr_{0.2}Fe_{0.8}Cr_{0.2}O_{3-\delta}$ under reducing conditions, Solid State Ionics, 139 (2001) 233-240.

[24] R.A. De Souza, J. Zehnpfenning, M. Martin, J. Maier, Determining oxygen isotope profiles in oxides with Time-of-Flight SIMS, Solid State Ionics, 176 (2005) 1465-1471.

[25] Netzsch, STA 449 F1 Jupiter, Product Brochure (2012).

[26] Kaisersberger, Netzsch Water Vapor Furnace and Humidity Generators, Manual (2008).

[27] C. Anghel, E. Hörnlund, G. Hultquist, M. Limbäck, Gas phase analysis of CO interactions with solid surfaces at high temperatures, Applied Surface Science, 233 (2004) 392-401.

[28] G. Hultquist, L. Gråsjö, Q. Lu, T. Åkermark, The analysis of gas consumption in the reaction of Fe and Cu in $H_2{}^{16}O/H_2{}^{18}O/O_2$ gas mixtures, Corrosion Science, 36 (1994) 1459-1471.

[29] T.N. Åkermark, G.B. Hultquist, L. Gråsjö, Probabilities for oxygen exchange in O_2 in contact with a solid surface, Journal of Trace and Microprobe Techniques, 14 (1996) 377-388.

[30] T.S. Bjørheim, PhD thesis, University of Oslo (2012).

[31] A. Magrasó, J.M. Polfus, C. Frontera, J. Canales-Vazquez, L.-E. Kalland, C.H. Hervoches, S. Erdal, R. Hancke, M.S. Islam, T. Norby, R. Haugsrud, Complete structural model for lanthanum tungstate: a chemically stable high temperature proton conductor by means of intrinsic defects, Journal of Materials Chemistry, 22 (2012) 1762-1764.

[32] D.G. Thomas, J.J. Lander, Hydrogen as a donor in zinc oxide, Journal of Chemical Physics, 25 (1956) 1136-1142.

[33] M. Kessel, R.A. De Souza, H.I. Yoo, M. Martin, Strongly enhanced incorporation of oxygen into barium titanate based multilayer ceramic capacitors using water vapor, Applied Physics Letters, 97 (2010) 021910/021911-021910/021913.

[34] J. Liu, R.J. Chater, R.J.H. Morris, S.J. Skinner, Oxygen surface exchange and diffusion studies of $La_2Mo_2O_9$ in different exchange atmospheres, Solid State Ionics, 189 (2011) 39-44.

[35] N. Sakai, K. Yamaji, T. Horita, Y.P. Xiong, H. Kishimoto, H. Yokokawa, Effect of water on oxygen transport properties on electrolyte surface in SOFCs. I. Surface reaction mechanism of

oxygen isotope exchange on solid oxide electrolytes, Journal of the Electrochemical Society, 150 (2003) A689-A694.

[36] R.N. Vannier, S.J. Skinner, R.J. Chater, J.A. Kilner, G. Mairesse, Oxygen transfer in BIMEVOX materials, Solid State Ionics, 160 (2003) 85-92.

[37] J.B. Smith, PhD thesis, University of Oslo (2005).

[38] V. Gil, J. Gurauskis, C. Kjoelseth, K. Wiik, M.-A. Einarsrud, Hydrogen permeation in asymmetric $La_{28-x}W_{4+x}O_{54+3x/2}$ membranes, International Journal of Hydrogen Energy, 38 (2013) 3087-3091.

[39] S. Erdal, PhD thesis, University of Oslo (2011).

[40] S. Hamakawa, L. Li, A. Li, E. Iglesia, Synthesis and hydrogen permeation properties of membranes based on dense $SrCe_{0.95}Yb_{0.05}O_{3-\alpha}$ thin films, Solid State Ionics, 148 (2002) 71-81.

[41] H. Yoon, T. Oh, J. Li, K.L. Duncan, E.D. Wachsman, Permeation Through $SrCe_{0.9}Eu_{0.1}O_{3-\delta}$/Ni-$SrCeO_3$ Tubular Hydrogen Separation Membranes, J. Electrochem. Soc., 156 (2009) B791-B794.

[42] R.A. Cox-Galhotra, S. McIntosh, Unreliability of simultaneously determining k chem and D chem via conductivity relaxation for surface-modified $La_{0.6}Sr_{0.4}Co_{0.2}Fe_{0.8}O_{3-\delta}$, Solid State Ionics, 181 (2010) 1429-1436.

[43] M.W. den Otter, H.J.M. Bouwmeester, B.A. Boukamp, H. Verweij, Reactor flush time correction in relaxation experiments, J. Electrochem. Soc., 148 (2001) J1-J6.

[44] J.A. Lane, J.A. Kilner, Measuring oxygen diffusion and oxygen surface exchange by conductivity relaxation, Solid State Ionics, 136-137 (2000) 997-1001.

[45] C.-R. Song, H.-I. Yoo, Chemical diffusivity of $BaTiO_{3-\delta}$ I. Experimental determination, Solid State Ionics, 120 (1999) 141-153.

[46] K. Yashiro, S. Akoshima, T. Kudo, M. Oishi, H. Matsumoto, K. Sato, T. Kawada, J. Mizusaki, Electrical conductivity and chemical diffusion in Perovskite-type proton conductors in H_2-H_2O gas mixtures, Solid State Ionics, 192 (2011) 76-82.

[47] R.A. De Souza, J.A. Kilner, Oxygen transport in $La_{1-x}Sr_xMn_{1-y}Co_yO_{3\pm\delta}$ perovskites Part II. Oxygen surface exchange, Solid State Ionics, 126 (1999) 153-161.

[48] J.A. Kilner, R.A. De Souza, I.C. Fullarton, Surface exchange of oxygen in mixed conducting perovskite oxides, Solid State Ionics, 86-88 (1996) 703-709.

[49] R. Merkle, J. Maier, H.J.M. Bouwmeester, A linear free energy relationship for gas-solid interactions: Correlation between surface rate constant and diffusion coefficient of oxygen tracer exchange for electron-rich perovskites, Angewandte Chemie, International Edition, 43 (2004) 5069-5073.